Journal of Computational Physics **148,** 23–58 (1999)
Article ID jcph.1998.6119, available online at http://www.idealibrary.com on IDEAL®

New Icosahedral Grid-Point Discretizations of the Shallow Water Equations on the Sphere

G. R. Stuhne and W. R. Peltier

Department of Physics, University of Toronto, Toronto, Ontario, Canada M5S 1A7
E-mail: gordan,peltier@atmosp.physics.utoronto.ca

Received April 14, 1998; revised September 9, 1998

We describe the implementation of numerical models of shallow water flow on the surface of the sphere, models which include the nondivergent barotropic limit as a special case. All of these models are specified in terms of a new grid-point-based methodology which employs an heirarchy of tesselations derivative of successive dyadic refinements of the spherical icosahedron. Among the potential advantages of such methods is the $\mathcal{O}(n)$ complexity in operation count that can be achieved for an n degree of freedom model if multigrid techniques are employed to solve the associated elliptic problems. Currently prevalent spectral transform models are, in contrast, $\mathcal{O}(n^2)$ complex due to the Legendre transform that must be performed to transform between spectral and grid-point representations of model fields at each time step. Using the new methodology, we have implemented two different formulations of each of the barotropic and shallow water dynamical systems. In one formulation, the vector velocity field is directly advanced in time; in the other, time integration is carried out entirely in terms of scalar quantities (i.e., absolute vorticity in the barotropic model and, in the more general shallow water model, height and velocity potential). We describe discretizations of the governing equations in which all calculations are performed in Cartesian coordinates in local neighbourhoods of the almost uniform icosahedral grid, a methodology that avoids potential mathematical and numerical problems associated with the poles in spherical coordinates. A number of standard numerical tests are performed with the resulting models and the results employed to compare them with each other and with previously published results obtained using other methodologies. Initial tests are performed for a standard suite that now constitutes the generally accepted benchmark for shallow water models on the sphere. The advantages and the disadvantages of the two shallow water formulations (vector and scalar) are contrasted and employed to demonstrate that the new icosahedral methodology is highly competitive with previously suggested grid-point models. The remaining results which we discuss relate to the process of erosion of a stratospheric polar vortex by a forced stationary Rossby wave disturbance, a physical problem which has previously been analyzed in detail in several well-known spectral transform simulations. It is shown that all of our models

0021-9991/99 $30.00

properly simulate this intensely nonlinear and computationally challenging physical process.

Key Words: shallow water equations; computational fluid dynamics; multigrid methods; refined icosahedral mesh; spherical domain; vortex erosion.

1. INTRODUCTION

The simulation of hydrodynamic flows in spherical geometry is a problem of computational fluid dynamics which is of great importance in many areas of physical science. In a recent paper (Stuhne and Peltier [1]) we addressed this problem and reported results obtained with a novel grid-point based numerical methodology that is well suited for integration of the partial differential equations that govern the evolution of such flows. The numerical framework developed therein was based upon a spatial discretization derived from the regular icosahedron and employed finite element multigrid methods (see, e.g., Hackbusch [2]) in the solution of the elliptic equation that arose in the nondivergent barotropic dynamical system that was our focus of interest in this initial stage of technical development. These fundamental building blocks, along with a number of additional algorithms employed to perform the operations of advection and numerical differentiation, were invoked to solve the inviscid, nondivergent two-dimensional barotropic vorticity equation (see, e.g., Pedlosky [3]). It was thereby demonstrated that the new numerical structure was effective in solving an important class of highly nonlinear inviscid fluid dynamical problems involving the cascade of structure to small scales. Specifically, we were able to accurately reproduce the well-known simulations of Juckes and McIntyre [4], who employed a conventional spectral transform model (see, e.g., Orszag [5]) to represent the dynamical process involved in the erosion of a polar vortex by an impinging Rossby wave. The new numerical structure was also tested by employing it to simulate the process of barotropic instability of a zonal flow with strong meridional shear and the subharmonic pairing interaction which thereafter ensues among the individual vortices generated by the primary instability.

The practical importance of the work described in Stuhne and Peltier [1], which we will herein extend to the significantly more challenging case of shallow water dynamics, lies primarily in the fact that grid-point models based upon the use of multigrid techniques have the potential to achieve a dramatic improvement in efficiency over the currently prevalent spectral transform models. Since this conventional methodology requires the computation of Legendre transformations between spectral and grid-point space at each time step, it has an operation count which is $\mathcal{O}(n^2)$ complex in the number of degrees of freedom, n (see Orszag [5]). In contrast, grid point models can be designed which are strictly $\mathcal{O}(n)$ complex, an improvement which has the potential to significantly extend the range of practically achievable spatial resolutions, since there will clearly be some threshold of n beyond which such methods remain viable after spectral transform methods have degraded to the point of being prohibitive in computational cost. Although this threshold has not yet been reached in practice, and although there are spectral transform schemes under development which promise a less dramatic nonlinear degradation of performance in n (see, e.g., Driscoll and Healy [6]), the rapid growth in the availability of computing resources and the inherently optimal $\mathcal{O}(n)$ complexity of grid-point methods suggests that such methods may soon be extremely useful, especially for applications requiring the maximum attainable resolution. The results presented in Stuhne and Peltier [1], for the case of nondivergent barotropic

dynamics, demonstrate explicitly that the expected optimal algorithmic complexity is, in fact, achieved in test cases which resolve physical processes that are significantly more complex than those manifested in the simpler tests to which numerical models are typically subjected.

Even beyond the theoretically expected improvement in efficiency at high spatial resolution, there are practical benefits in the use of an entirely grid-point-based methodology. For example, such methods allow one to avoid the anomalous oscillations which are associated with Gibbs phenomena in spectral transform models and also provide an inherently more natural representation for local features such as mountains. Spectral transform models, moreover, perform key numerical operations in a Gaussian grid-point domain, over which there is a dramatic spatial inhomogeneity which wastefully over-resolves polar regions (and can lead to numerical problems if some form of atypical forcing and/or dissipation must be applied in a particular analysis). This last shortcoming can be ameliorated in spectral transform models if one employs reduced Gaussian grids (e.g., Hortal and Simmons [7]), but doing so disrupts the exact calculation of quadratic terms which is one of the key advantageous features of such models. It can be circumvented almost entirely in grid-point-based methodologies provided that one employs a mesh structure which "tiles" the sphere in an approximately uniform fashion. In geometric terms, there are, of course, no perfectly uniform tesselations of this domain except for the exact spherical projections of the so-called Platonic solids (i.e., tetrahedra, cubes, octahedra, etc.). As early as the 1960s, Williamson [8] and Sadourny *et al.* [9] experimented with nondivergent barotropic models of inviscid fluid flow discretized on grids which were derived from the approximately uniform grid generated by the spherical projection of the regular icosahedron (which is, with 20 sides, the most complex Platonic solid). The nondivergent barotropic model of Stuhne and Peltier [1] employs a similar grid structure which was originally devised by Baumgardner and Frederickson [10] in the context of their studies of thermal convection in a three-dimensional spherical shell at infinite Prandtl number. This particular mesh offers a number of numerical advantages, most notably by virtue of the fact that successive subdivisions of the primary icosahedral discretization are performed in a recursive way which facilitates the application of multigrid methods and allows for the specification of natural finite element coordinates on spherical triangles. The model described in Stuhne and Peltier [1] invokes a combination of finite element and finite difference techniques designed specifically for this grid in such a way as to obtain an $\mathcal{O}(n)$ complex hybrid algorithm with which to advance the solution in time. This methodology represents a very significant improvement over the early efforts of Williamson [8] and Sadourny *et al.* [9], which did not incorporate multigrid techniques as these had yet to be invented.

As the simplest one layer model of fluid flow which supports complex nonlinear dynamics and a turbulent "cascade," the nondivergent barotropic model is of considerable physical interest in and of itself. It is therefore rational to begin the assessment of the applicability of any body of numerical methodology with analyses based upon it (as Williamson [8], Sadourny *et al.* [9], and we ourselves have done). The dynamics, however, derive from the assumption that divergence and divergence tendency vanish identically. These assumptions entirely suppress the appearance of fast gravity waves, whose existence, as is well known, may lead to computational instabilities resulting from temporal aliasing in the numerical models appropriate for global atmospheric, oceanographic, and astrophysical simulations. In contrast, shallow water models, which also apply to the evolution of a single layer of fluid, treat the thickness of this layer as a dynamically varying field and thus admit a

representative spectrum of linear and nonlinear wave phenomena and of their associated numerical artifacts (see, e.g., Pedlosky [3]). Consequently, implementation of this more complex representation of fluid flow has become the *de facto* standard test to which any numerical methodology intended for subsequent use in full three-dimensional models on the sphere must be subjected. For this reason, Williamson *et al.* [11] proposed a standard suite of tests whereby different shallow-water models in spherical geometry might be evaluated and compared in a variety of physical configurations. Although these tests manifest physical behavior which is considerably less challenging to resolve than that which was considered for test purposes with the nondivergent barotropic model in Stuhne and Peltier [1], they are nevertheless extremely valuable in providing standard points of comparison between numerical methodologies. It is to be hoped that further tests such as our own might also be adopted as additional standards which are more completely representative of the full physical complexity realizable in one-layer hydrodynamic models. In the analyses to follow, we will both describe and extend the basic numerical techniques employed in the nondivergent barotropic model of Stuhne and Peltier [1] both to the shallow water simulation of the complex cases considered therein and to a selection of the standard shallow water tests of Williamson *et al.* [11].

Cullen [12], in one of the earliest examples of work in this area and, more recently, Masuda and Ohnishi [13] and Heikes and Randall [14, 15] have also described the implementation of shallow water models in spherical geometry employing grid structures which are related to the regular icosahedron. All of the grid structures employed by these authors, however, differ in significant respects from that of Baumgardner and Frederickson [10] which we have elected to employ. Strictly speaking, Cullen's [12] mesh structure cannot be said to be derived from the spherical icosahedron at all, since the basic figure is initially distorted so as to subdivide the sphere into three latitudinally distinct regions (a subdivision which is realized only approximately in the Platonic figure). Masuda and Ohnishi [13], on the other hand, begin with a proper icosahedron, but employ a nonrecursive means of subdividing spherical triangles to obtain higher resolution grids. Heikes and Randall [14, 15] employ an icosahedral basic grid and a recursive procedure of dyadic subdivision but apply a "twist" in such a way as to force the mesh to be symmetric about the equator (arguing that it is desirable for the numerical representation of idealized flows with cross-equatorial symmetry to retain this property). Furthermore, these authors discretize the problem in such a way that the grid is defined in terms of pentagonal and hexagonal Voronoi cells on the sphere rather than in terms of triangular facets (see, e.g., Augenbaum and Peskin [16]). Whether or not the "twist" which Heikes and Randall [14, 15] apply to their grid is a desirable feature is largely an aesthetic issue. Nothing is gained in terms of formal accuracy over the dyadically refined icosahedron which we employ while there is likely to be some additional complexity of computer code required to implement the "twisted" grid. Our own inclination is to prefer the most natural geometrical and logical structure delivered by the Platonic solid itself and to treat the degree of cross-equatorial asymmetry in an ideally symmetric flow as an indication of numerical error which might be camouflaged if symmetry were imposed. In any event, physically realized flows in nature never manifest precise cross-equatorial symmetry.

Of greater significance than these details of the icosahedron-based grid structure is the choice of the mathematical form of the shallow-water equations to be employed and the discrete approximation of them on the appropriate grid. Various formulations of the shallow-water dynamical system were, in fact, presented and compared in Williamson *et al.* [11]. Of the icosahedron-based models, those described by Masuda and Ohnishi [13] and Heikes and

Randall [14, 15] employ the streamfunction, velocity potential formulation of the equations. Layer thickness, h^*, and absolute vorticity, η, both evolve in time according to simple conservation laws of flux form, namely (with Φ representing either h^* or η),

$$\frac{\partial \Phi}{\partial t} + \nabla \cdot (\mathbf{u}\Phi) = 0, \tag{1}$$

while the horizontal divergence of flow velocity, $\delta = \nabla \cdot \mathbf{u}$, is governed by a similar but somewhat more complex equation. The system is dynamically closed because the streamfunction, ψ, and velocity potential, χ, may be obtained, respectively, from η and δ through the solution of associated elliptic problems and may, in turn, be employed in the *a posteriori* diagnosis of a numerical approximation for **u** (see below). This is simply the shallow-water extension of the form of the nondivergent barotropic equation employed by Williamson [8], Sadourny *et al.* [9], and Stuhne and Peltier [1] (we will continue to employ the symbol $Q \equiv \eta$ to denote the absolute vorticity in what follows). However, in discretizing the nondivergent barotropic and full shallow-water equations, Williamson [8], Sadourney *et al.* [9], Masuda and Ohnishi [13], and Heikes and Randall [14, 15] all rely upon the fact that scalar advection in two dimensions may be cast in terms of specific Jacobian and flux operators in a way which allows one to avoid the explicit computation of the velocity vector, **u**, in the course of a numerical advection step. It is therefore unclear how any of these models would incorporate the additional numerical operations required in fully three-dimensional flow models. Furthermore, even in 2D integrations, these methods estimate a particular term in the shallow-water divergence equation by applying discrete differential operators iteratively (rather than by invoking a proper Taylor series-based stencil), a procedure which could potentially lead to difficulties. The basic body of numerical methodology developed and invoked in Stuhne and Peltier [1], in contrast, is considerably more versatile in these respects since computational stencils are derived in grid-point space under assumptions which allow for the consistent discretization of much more general terms. A similar approximation technique was subsequently derived by Swarztrauber *et al.* [17] and referred to as the "Cartesian method."

Considering further the issue of the extension of a shallow-water model to the case of fully three-dimensional flow, there is a difficulty inherent in the use of entirely scalar prognostic variables as in the streamfunction-velocity potential formulation. It is true that atmospheric models generally treat the vertical velocity as an independent component to be diagnosed according to the hydrostatic balance relation, thus allowing for scalar variables to be retained in the representation of the horizontal flow (see, e.g., Bourke [18] and Hoskins and Simmons [19]). There are, however, significant geophysical phenomena, particularly in the vicinity of the equator, for which an inherently nonhydrostatic representation is required (see DeVerdière and Schopp [20]). Under such conditions, the mathematical decomposition of tangential velocity into two scalar fields, where possible at all, becomes considerably more complex. Shallow-water models based upon a full primitive variable vector formulation will, in contrast, generalize to these cases in a relatively straightforward way. Of the shallow water models mentioned, the one developed by Cullen [12] utilizes this formulation, which can, however, give rise to its own problems. Most notably, due to the underlying curvature of the spherical geometry, the advective form of the shallow water dynamical system includes metric terms which diverge at the singularities of whatever coordinate system is chosen (usually spherical polar coordinates). This introduces pole problems above and beyond those that would be associated with grid spacing and may account for some of

the numerical difficulties mentioned by Cullen [12] and which have prevented his methodology from gaining wider acceptance despite its being based upon the use of an almost homogeneous grid. As Cullen [12] has also discussed, a further problem may lie in the fact that first-order finite elements were employed in the discretization of the equations, which is a very low-accuracy spatial approximation. The methods formulated in Stuhne and Peltier [1] avoid the latter difficulty entirely by invoking a second-order spatial Taylor series approximation. Moreover, when combined with the constrained three-dimensional formulation of the shallow-water equations due to Côté [21] (see below), our framework can accomodate a discretization in which the velocity, **u**, is integrated without requiring the computation of metric terms. The only evident disadvantage of adopting a constrained velocity formulation is the additional computer memory required to store a mathematically superfluous third velocity component in shallow-water dynamics. This is, however, not a problem on modern computers, given the large increases of available memory that have occurred as memory cost has dramatically fallen.

As may be inferred on the basis of the above commentary, the basic body of numerical methodology originally applied by Stuhne and Peltier [1] to nondivergent barotropic dynamics is sufficiently versatile to enable us to implement shallow-water models in spherical geometry which are based on either scalar or vector prognostic variables. One can, as we will discuss, also devise a vector version of the nondivergent barotropic model described in Stuhne and Peltier [1], which is, like the nondivergent barotropic models of Williamson [8] and Sadourney *et al.* [9], based on the scalar advection of absolute vorticity. We therefore have effective numerical means at our disposal of comparing the relative merits of vector and scalar formulations of a given one-layer model as well as the behaviours of the nondivergent barotropic and full shallow-water one-layer representations of the same physical system (it being expected that the former should be recovered as a limit of the latter under appropriate scaling conditions). The main objective of this study, and its primary novelty, is in addressing these issues in the physical context of cases presented in Stuhne and Peltier [1] as well as in the standard test set of Williamson *et al.* [11]. As will be evident from our discussion, although there has been significant attention in the recent literature to scalar shallow-water models on icosahedral grids, little consideration has been given to the alternative vector formulations which are realizable on the same mesh. The derivation of a vector-based shallow-water equations model with our earlier local approximation methods and its application to problems with significant dynamics is therefore something of a novelty in and of itself. As we took pains to stress in Stuhne and Peltier [1], our own efforts are not, at the present stage, intended either to be competitive with existing production models, based upon the spectral transform methodology, or to represent implementations of any of the possible alternative formulations of shallow water or nondivergent barotropic dynamics with optimized algorithmic subcomponents. What we do aim to establish, rather, is an objective basis for comparing these alternatives and for ascertaining the most fruitful avenues for further development. This being said, however, it will be seen that the results achieved can be quite competitive with those hitherto published for other icosahedral grid-point models, a fact which will be seen to fully justify the fundamental principles upon which our approach is based.

In Section 2 of what follows, we discuss both the shallow water and nondivergent barotropic dynamical systems and the initial conditions to be employed in their integration in a way which develops several of the themes mentioned in this Introduction in greater technical detail. In Section 3, we will briefly review the various numerical methods originally

developed in Stuhne and Peltier [1] and discuss the extensions required for application to the more general case of shallow water dynamics. In Sections 4 and 5 we present and discuss the results of analyses obtained with the new numerical methodology applied, respectively, to the standard test cases of Williamson *et al.* [11] and to the more challenging problem of Rossby wave-induced vortex erosion. Concluding remarks are offered in Section 6.

2. MODEL EQUATIONS

The basic structure of the physical problem that is analyzed in shallow-water dynamics is that of horizontal flow within a layer of fluid having a dynamically varying height and a static underlying topography. The mathematical formulation of the problem may therefore be cast in terms of a two-component vector velocity field, (u_1, u_2), and a scalar height field, $h = h^* + h_s$, in which h^* is the dynamically varying component and h_s is the static topography. On the sphere, of course, the fluid layer height and the topography may be thought of as constituting perturbations to a closed surface whose curvature requires that the general velocity vector, $\mathbf{u} = u_1\mathbf{e}_1 + u_2\mathbf{e}_2$, be expanded in terms of a basis, $\{\mathbf{e}_1(\mathbf{x}), \mathbf{e}_2(\mathbf{x})\}$, which varies with position. For practically useful coordinate systems (e.g., spherical polar coordinates) the resulting dynamical equations include Christoffel symbols which diverge at the singularities of the mapping (e.g., at the poles). Fortunately, there are at least two relatively straightforward schemes whereby the potential problems resulting from this may be obviated, one of which preserves the vector character of the dynamics, while the other transforms the flow to one described in terms of the evolution of scalar fields.

2.1. *Vector Form*

Côté [21] has described a formulation in which shallow-water flow on the sphere is treated as a constrained instance of a general 3D flow. Specifically, the velocity vector field is expanded in terms of three components, u_x, u_y, and u_z, such that

$$\mathbf{u} = u_x\mathbf{e}_x + u_y\mathbf{e}_y + u_z\mathbf{e}_z, \tag{2}$$

where $\mathbf{e}_x$, $\mathbf{e}_y$, and $\mathbf{e}_z$ are (constant) unit vectors along the Cartesian x-, y-, and z-axes. This requires that an extra field be introduced, but it eliminates all singularities and, furthermore, it will be seen, all asymmetries in the roles played by the components of $\mathbf{u}$ in the vector evolution equation. In terms of the three components u_x, u_y, and u_z, this evolution equation is, of course, underdetermined on the 2D spherical surface and requires that an additional constraint be appropriately imposed so as to ensure that

$$\mathbf{x} \cdot \mathbf{u} = xu_x + yu_y + zu_z = 0 \tag{3}$$

for all $\mathbf{x}$ and for all time. When nondimensionalized on the rotating sphere, the resulting shallow-water dynamical system, as originally analyzed by Côté, takes the form

$$\frac{\partial \mathbf{u}}{\partial t} + (\mathbf{u} \cdot \nabla)\mathbf{u} + R_0^{-1}(z + F)\mathbf{x} \times \mathbf{u} = -F_0^{-2}\nabla h - (\mathbf{u} \cdot \mathbf{u})\mathbf{x} \tag{4}$$

$$\frac{\partial h^*}{\partial t} + \nabla \cdot (h^*\mathbf{u}) = 0, \tag{5}$$

wherein the last term of Eq. (4) is a centripetal force whose influence is such as to keep fluid particles confined to the unit spherical surface defined by

$$\mathbf{x} \cdot \mathbf{x} = x^2 + y^2 + z^2 = 1. \tag{6}$$

In addition to variables already defined, the system (4)–(5) includes the nondimensional external scaling parameters R_0 (a Rossby number) and F_0 (a Froude number), which are defined, respectively, as

$$R_0 = \frac{U}{2\Omega_0 r_s} \tag{7}$$

and

$$F_0 = \frac{U}{\sqrt{gH}}. \tag{8}$$

In these definitions, r_s and Ω_0 are the radius and angular frequency of the rotating sphere, g is the surface gravitational acceleration, U is a characteristic velocity in the rotating frame, and H is a characteristic fluid layer depth. If one imposes the requirement that U be of a magnitude such as to make the nondimensional $\mathbf{u}$ field $\mathcal{O}(1)$ in amplitude in the rotating frame (and thus essentially defines U in terms of the global kinetic energy of the flow), then the parameter R_0 directly constrains the structure of admissible dynamical fields. However, if, as is the case in the analyses to be considered in this study, the exact form of the velocity field is specified *a priori*, then R_0 plays no rôle in the physical definition of the problem and can simply be set in such a way as to put the nondimensional equations into a convenient form. For present purposes, it will suffice to choose $U = 2\Omega_0 r_s$ (i.e., $R_0 = 1$) and then to consider the dynamics to be controlled entirely by a new Froude number

$$F_0 = \frac{2\Omega_0 r_s}{\sqrt{gH}}. \tag{9}$$

In terms of physical applications, it is interesting to observe that, provided the nondimensional parameters are suitably re-interpreted, Eqs. (4) and (5) have a form equivalent to the 2D compressible Euler equations. This fact has been exploited in drawing analogies between these two otherwise dissimilar physical systems (e.g., in Ford's [22] application of Lighthill's [23] aerodynamic sound generation theory to gravity waves).

It should be noted that the z-coordinate that appears explicitly in Eq. (4) corresponds to the latitudinal variation of the Coriolis parameter ($\cos\theta$ in terms of colatitude). Some of the numerical tests that we will perform call for an angular displacement between the rotational and computational poles and for these cases the appropriate transformation is easily obtained. The function F which perturbs z in Eq. (4) represents a quasi-topographic forcing that we will, for some purposes, take to be of the form

$$F(\mathbf{x}, t) = \frac{0.3x\,A(t)\,B(\cos^{-1} z)}{\sqrt{x^2 + y^2}}, \tag{10}$$

which is equivalent to that assumed in the analyses of Juckes and McIntyre [4]. The forms of the functions A and B are illustrated in Stuhne and Peltier [1], wherein we described the

application of a nondivergent barotropic version of the model to the reproduction of Juckes and McIntyre's results. Further comparisons pertaining to this test case will be presented in what follows, all of which will be based upon the use of the same form for F. For the purposes of other analyses, we will set $F = 0$.

2.2. *Scalar Form*

By taking the divergence and curl of the momentum equation, the system (4)–(5) may be recast into the equivalent form,

$$\nabla^2 \left(\frac{\partial \chi}{\partial t} + F_0^{-2} h + \frac{1}{2} \mathbf{u} \cdot \mathbf{u} \right) = (Q - z - F) Q - \mathbf{x} \cdot (\mathbf{u} \times \nabla Q) \tag{11}$$

$$\frac{\partial Q}{\partial t} = -\nabla \cdot (Q \mathbf{u}) \tag{12}$$

$$\frac{\partial h^*}{\partial t} = -\nabla \cdot (h^* \mathbf{u}), \tag{13}$$

in which the velocity vector field may be obtained in terms of a streamfunction, ψ, and a velocity potential, χ, by means of the relation

$$\mathbf{u} = \nabla \times (\mathbf{x} \psi) + \nabla \chi. \tag{14}$$

The absolute vorticity, Q, evolves according to a conservation law of flux form (Eq. (12)), of the same form as that which governs h^*, as previously mentioned. The time evolution of these two quantities may therefore be determined on the basis of a suitable advection scheme and the streamfunction, ψ, that is required to determine the velocity in such a scheme, may be inferred from the absolute vorticity by inverting the Poisson equation,

$$\nabla^2 \psi = -Q + z + F. \tag{15}$$

In this formulation of the shallow water model the dynamics are thus described entirely in terms of the evolution of the scalar quantities, Q, h^*, and χ, thus providing an alternative means of avoiding problems associated with the underlying curvature of spherical geometry (there being no Christoffel symbols arising in spatial derivatives of scalars).

By inverting the Laplacian operator in Eq. (11) to directly obtain the time-tendency of the velocity potential, $\partial \chi / \partial t$, one may avoid having to compute any numerical derivatives higher than first order. In contrast, evolving the divergence, $D = \nabla^2 \chi$, as is done, for instance, by Heikes and Randall [14, 15], necessitates the numerical estimation of the second-order operator $\nabla^2 (\frac{1}{2} \mathbf{u} \cdot \mathbf{u})$ after a first-order numerical derivative (as per Eq. (14)) has already been invoked in the calculation of $\mathbf{u}$. The effective differentiation stencil therefore derives from multiple passes over the data, rather than from a proper Taylor series expansion optimized to the local grid structure. Such a device (which we also use to approximate the ∇^6 hyperdiffusion operator in Section 3.4 below) can potentially give rise to distortions and should, if possible, be avoided in the discretization of the key dynamical terms in a model. The algorithm implied by the form of Eqs. (11)–(13) may allow one to avoid this potential difficulty, but not in all circumstances. Most notably, the advantage gained does not necessarily continue to apply to time-stepping schemes deriving from the so-called *semi-implicit* formulation in which the height field is expanded about an arbitrary reference in such a

way as to minimize the aliasing of fast, grid-scale gravity wave propagation by the choice of time step (see Kwizak and Robert [24]; Robert *et al.* [25]). This is the case because, in contradistinction to explicit schemes, the $i+1$ time level of a semi-implicitly defined field Φ cannot be directly determined through a simple diagnosis of $\partial\Phi/\partial t$ at previous time levels i, $i-1$, etc.

Semi-implicit schemes may be devised for both the vector and the scalar formulations of the shallow water equation system and theoretically allow for time steps to be several times larger than in explicit time-stepping schemes (the latter being limited by the phase speed of effectively numerical gravity waves rather than merely by the CFL criterion on advection velocity). Greater, although still not unconditional, numerical stability is thus achieved at the cost of distorting the physics at scales close to that of the grid. The implementation of these methods, moreover, generally entails the solution of elliptic equations of a form similar to those which must be solved in the scalar icosahedral models of Masuda and Ohnishi [13] and Heikes and Randall [14, 15], as well as in our Eqs. (11)–(13). Consequently, it is likely that these models, which must already bear the computational cost of elliptic inversions, would, on the whole, be accelerated by semi-implicit methods. This is not, however, necessarily true of our vector shallow-water model, since, as is clear from our Eqs. (4)–(5), direct integration of the primitive variable form of the shallow-water equations using the explicit technique should be a relatively efficient numerical operation on any grid. The vector-explicit scheme may therefore allow one to reproduce a simulation performed using a semi-implicit vector model (or any scalar model) at comparable operation count even though significantly smaller time steps must be employed. In any case, it is of benefit to establish a basis for comparison by first implementing new numerical discretizations in fully explicit mode, since the direct resolution of relevant physical processes in this way precludes the possibility that aphysical distortions associated with an implicit scheme might produce misleading results. The previous models cited above all employ explicit time-stepping schemes and we will adhere to this precedent.

Therefore, we will focus in the present paper on the implementation and comparison of various explicit formulations of shallow-water dynamics. Aside from its modifying the typical sequence of numerical operations, one of these formulations, as expressed in Eqs. (11)–(13), represents the same basic process of scalar integration and elliptic inversion which has been invoked in the previously cited studies. It is of interest, therefore, to consider how results obtained under this new discretization compare with results from other scalar shallow-water models, as well as with results from a new vector shallow-water model which we have also devised on the basis of the same numerical techniques. Given the versatility of our basic methods, any of a number of such models can be practically implemented with them and possibly extended to the simulation of full 3D flows (our vector formulation, indeed, is already derived through the constraint of a 3D flow to the surface). In practical terms, the only sure means of assessing the relative merits of the alternative formulations is through the direct comparison of the results obtained by applying them to specific problems of interest.

2.3. *The Nondivergent Barotropic Model*

Assuming the flow to be nondivergent for all time (i.e., setting $D = \nabla^2\chi \equiv 0$) yields what is commonly referred to as the (nondivergent) barotropic model (see, e.g., Pedlosky [3]), which is, in dynamical terms, the simplest possible representation of one-layer flow. In this

limit, χ is everywhere an undetermined (and irrelevant) constant and Eq. (14) for $\mathbf{u}$ assumes the simpler form,

$$\mathbf{u} = \nabla \times (\mathbf{x}\psi). \tag{16}$$

Together with the Q-advection equation (12) and the Poisson equation (15), this defines a closed scalar model based solely upon the dynamical process of absolute vorticity advection in which the height field, h, need never be explicitly considered. The implementation of this model using the new numerical framework was described in detail in Stuhne and Peltier [1]. Where it is required, h can be diagnosed from the other fields if one imposes the balance condition of Charney [26], substituting $\partial\chi/\partial t = 0$ into Eq. (11), and thereby obtaining

$$h = H_0 + F_0^2\left\{-\frac{1}{2}\mathbf{u}\cdot\mathbf{u} + \nabla^{-2}[(Q - z - F)Q - \mathbf{x}\cdot(\mathbf{u}\times\nabla Q)]\right\}, \tag{17}$$

in which ∇^{-2} denotes the inverse Laplacian operator and H_0 is an undetermined constant. Some value of the constant H_0 must be supplied as an external parameter, but it is to be expected on *a priori* grounds that $H_0 \sim 1$, in order to maintain consistency with the choice of height scale H in the determination of the Froude number in Eq. (9). For nondivergent $\mathbf{u}$, the resulting h is the balanced height field about which small amplitude shallow-water fluctuations would propagate as gravity waves. Gravity wave effects are, of course, suppressed in the nondivergent barotropic model, wherein the variation of F_0 has no *dynamical* implications. Substitution of the expression (17) for h into the height field evolution equation (13) will establish that nondivergent barotropic dynamics may be realized as a limiting case of shallow water dynamics when F_0 is small (corresponding to the limit of infinitely fast gravity wave propagation).

If we take the divergence of Eq. (4) for a nondivergent barotropic flow, we derive an alternative expression, namely

$$\nabla^2\left(F_0^{-2}h\right) = -\nabla\cdot\left\{(\mathbf{u}\cdot\nabla)\,\mathbf{u} + R_0^{-1}\,(z+F)\,\mathbf{x}\times\mathbf{u} + (\mathbf{u}\cdot\mathbf{u})\,\mathbf{x}\right\}, \tag{18}$$

by which the weighted balanced height field, $F_0^{-2}h$, is diagnosable directly from $\mathbf{u}$ at any time level. In combination with the vector momentum equation (4), this defines a vector formulation of the nondivergent barotropic model (recognizing that the F_0 value and the constant background height are irrelevant). We therefore have both vector and scalar forms of each of the shallow water and nondivergent barotropic dynamical systems. These will be of use to us in making a variety of intercomparisons to be described in what follows.

2.4. *Initial Conditions*

In most of the cases to be discussed, the initial form of the flow will be taken to be both nondivergent and balanced and therefore fully specified in terms of an initial barotropic potential vorticity field, $Q_0(\mathbf{x})$, from which the $\mathbf{u}_0$ field may be obtained by means of Eqs. (15) and (16). The corresponding balanced height, h_0, may then be derived from Eq. (17) with a suitable choice of H_0. For such initial conditions, the various shallow-water and nondivergent barotropic formulations which we have discussed may be initialized so as to have numerically identical $\mathbf{u}$ and h fields. They will, of course, diverge in the course of their subsequent evolution and it will be of interest to us to consider in this way the

comparative behaviours of the different models which can be devised within our basic numerical framework. In one instance, a simulation must be initialized with a more general divergent flow and in this case (which will only be analyzed using the vector form of the shallow water equations) we simply set the fields $\mathbf{u}_0$ and h_0 according to the prescribed initial conditions.

3. NUMERICAL METHODS

Many of the details of the spatial discretization, data structures, and numerical algorithms required to perform the numerical operations relevant to this study have already been discussed in some detail in Stuhne and Peltier [1]. In this section, we will therefore limit the discussion to providing a brief summary of the main ingredients previously described and for the most part will focus on the extensions of this work required in the present shallow-water context.

3.1. *Grid Structure*

In terms of the mathematical notation developed by Stuhne and Peltier [1], the definition of the grid structure of Baumgardner and Frederickson [10] proceeds from the basic spherical icosahedron, or level 0 grid, as follows. The Platonic figure consists of 20 identical spherical triangles, each of which we denote by $\mathcal{T}^0_{i,j,k}$. Referenced by the three indices i, j, and k (whose order of occurrence is unimportant in our notation) are three points, $\mathcal{P}^0_i$, $\mathcal{P}^0_j$, and $\mathcal{P}^0_k$, which define the vertices of the triangle. The boundary of the triangular region, $\partial\mathcal{T}^0_{i,j,k}$, is defined by three arcs, $\mathcal{A}^0_{i,j}$, $\mathcal{A}^0_{i,k}$, and $\mathcal{A}^0_{j,k}$, which are the geodesic curves connecting pairs of vertices. A *dyadic refinement* from grid level l to grid level $l+1$ entails the subdivision of each arc in such a way as to enhance the number of points in the finer grid by the number of arcs in the coarser one. Each triangle of the level l grid is, moreover, subdivided into four subtriangles by additional geodesic arcs which link these bisectors. Starting from the spherical icosahedron as grid level 0, this process of dyadic subdivision recursively determines a mesh at arbitrary level l which has $10n^2+2$ grid points, where $n=2^l$ (see Stuhne and Peltier [1]). The hierarchy of grids thus generated is best illustrated graphically, and in Fig. 1 we therefore show the mesh structures of grid levels 0 through 6 that result from the above described construction. For the purpose of organizing the data in computer memory, it is convenient to logically subdivide the basic icosahedron into 10 diamonds consisting of pairs of facets. One can thus arrange the points of grid level l into 10 $n \times n$ logical square arrays and two outliers at the north and south poles. In order to further facilitate data manipulation, a `FORTRAN` array of dimensions $(0:n+1, 0:n+1, 10)$ is used to index each field, extra edge cells for a given diamond being employed to store copies of values from neighbouring diamonds (values which are updated at appropriate points in the computation). The values at northern and southern polar nodes are stored in the respective locations (0, 1, 1) and (0, 1, 6). The exact geometric layout of the data is fully described in Stuhne and Peltier [1].

3.2. *Numerical Spatial Derivatives*

Denoting by $\mathbf{x}^l_i$ the 3D position vector at point $\mathcal{P}^l_i$ of grid level l and by $\mathcal{F}^l_i$ an arbitrary scalar or vector field evaluated at that point, our numerical methodology frequently requires

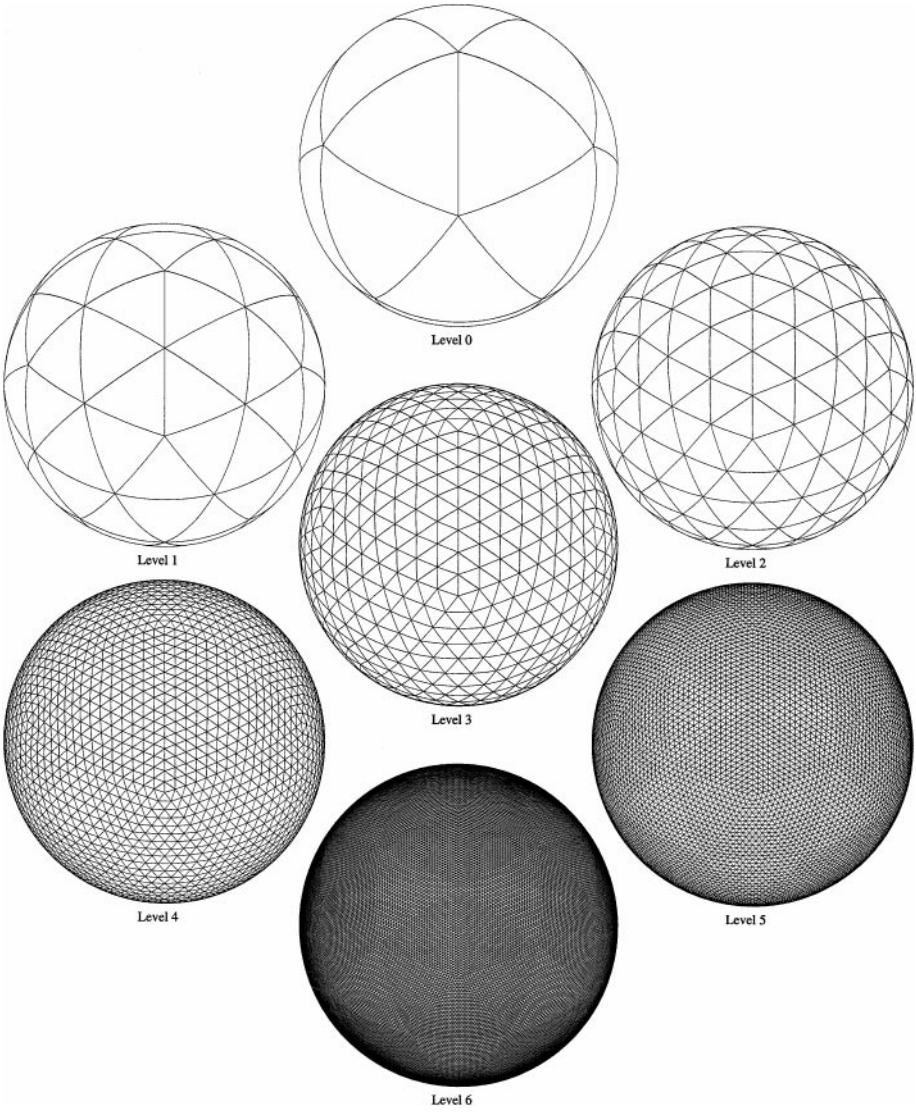

FIG. 1. Dyadically refined spherical icosahedral mesh structures at grid levels 0 through 6.

the explicit estimation of $(\mathcal{D}\mathcal{F})_i^l$, where $\mathcal{D}$ is a continuous differential operator acting upon the undiscretized field $\mathcal{F}(\mathbf{x})$. The general form of an approximation for $(\mathcal{D}\mathcal{F})_i^l$ may be written as

$$(\mathcal{D}\mathcal{F})_i^l \approx \sum_j \mathcal{D}_{ij}^l \left(\mathcal{F}_j^l - \mathcal{F}_i^l\right), \tag{19}$$

in which $\mathcal{D}_{ij}^l$ is a sparse matrix or operator array which is nonzero only for i, j such that $|\mathbf{x}_j^l - \mathbf{x}_i^l|$ is small. On the icosahedral grid, it is both natural and practical to consider a neighbourhood of each point $\mathcal{P}_i^l$ consisting of the point and immediate neighbours, $\mathcal{P}_j^l$, linked to it by geodesic arcs $\mathcal{A}_{i,j}^l$. A local approximation to $\mathcal{F}(\mathbf{x})$ on grid level l in the neighbourhood of $\mathcal{P}_i^l$, which we denote by $\tilde{\mathcal{F}}_i^l(\mathbf{x})$, is then assumed to take the second-order

form

$$\tilde{\mathcal{F}}_i^l(\mathbf{x}) = \mathcal{F}_i^l + \tilde{\mathcal{F}}_{i,1}^l s + \tilde{\mathcal{F}}_{i,2}^l t + \frac{1}{2}\tilde{\mathcal{F}}_{i,3}^l s^2 + \tilde{\mathcal{F}}_{i,4}^l st + \frac{1}{2}\tilde{\mathcal{F}}_{i,5}^l t^2, \tag{20}$$

in which

$$s = \mathbf{v}_i^l \cdot \left(\mathbf{x} - \mathbf{x}_i^l\right), \quad t = \mathbf{w}_i^l \cdot \left(\mathbf{x} - \mathbf{x}_i^l\right) \tag{21}$$

are 2D affine coordinates on the tangent plane at $\mathcal{P}_i^l$. The 3D vectors $\mathbf{v}_i^l$ and $\mathbf{w}_i^l$ are defined as

$$\mathbf{v}_i^l = \frac{\mathbf{b}_i^l \times \mathbf{x}_i^l}{\left(\mathbf{b}_i^l \times \mathbf{x}_i^l\right) \cdot \mathbf{a}_i^l}, \quad \mathbf{w}_i^l = \frac{\mathbf{a}_i^l \times \mathbf{x}_i^l}{\left(\mathbf{a}_i^l \times \mathbf{x}_i^l\right) \cdot \mathbf{b}_i^l}, \tag{22}$$

in which $\mathbf{a}_i^l$ and $\mathbf{b}_i^l$ are the basis vectors of the local tangential coordinate system and are given by the expressions

$$\mathbf{a}_i^l = \mathbf{x}_j^l - \mathbf{x}_i^l\left(\mathbf{x}_i^l \cdot \mathbf{x}_j^l\right), \quad \mathbf{b}_i^l = \mathbf{x}_k^l - \mathbf{x}_i^l\left(\mathbf{x}_i^l \cdot \mathbf{x}_k^l\right), \tag{23}$$

wherein $\mathbf{x}_j^l$ and $\mathbf{x}_k^l$ are the coordinates of two neighbouring points chosen such that $\mathcal{P}_i^l$, $\mathcal{P}_j^l$, and $\mathcal{P}_k^l$ are not all on the same geodesic. From these formulae, it follows (see Stuhne and Peltier [1]) that the gradient and Laplacian of the local approximation may be obtained as

$$\nabla\tilde{\mathcal{F}}_i^l(\mathbf{x}) = \tilde{\mathcal{F}}_{i,1}^l \mathbf{v}_i^l + \tilde{\mathcal{F}}_{i,2}^l \mathbf{w}_i^l \tag{24}$$

and

$$\nabla^2\tilde{\mathcal{F}}_i^l(\mathbf{x}) = \tilde{\mathcal{F}}_{i,3}^l\left|\mathbf{v}_i^l\right|^2 + 2\tilde{\mathcal{F}}_{i,4}^l \mathbf{v}_i^l \cdot \mathbf{w}_i^l + \tilde{\mathcal{F}}_{i,5}^l\left|\mathbf{v}_i^l\right|^2. \tag{25}$$

The five coefficients $\tilde{\mathcal{F}}_{i,\alpha}^l$ must be linearly related to $\mathcal{F}_j^l - \mathcal{F}_i^l$ for a valid approximation to result which effectively determines the $\mathcal{D}_{ij}^l$ of Eq. (19). However, since all points but those lying on the level-0 icosahedron have six (rather than five) neighbours, the $\tilde{\mathcal{F}}_{i,\alpha}^l$ values are generally overdetermined. We therefore obtain them by minimizing the quantity

$$\Delta \equiv \sum_j \left\|\tilde{\mathcal{F}}_i^l\left(\mathbf{x}_j^l\right) - \mathcal{F}_j^l\right\|^2, \tag{26}$$

which results in the linear problem discussed in Stuhne and Peltier [1].

When spatially discretized according to this procedure, the vector form of the shallow-water evolution equations given by Eqs. (4)–(5) may be written as

$$\frac{\partial \mathbf{V}_i^l}{\partial t} = \left(-\mathbf{R}_i^l, -S_i^l\right), \tag{27}$$

in which the four-component vector $\mathbf{V}_i^l$ is defined as $(\mathbf{u}_i^l, h_i^{*l})$ and the $\mathbf{R}_i^l$ and S_i^l components in the RHS are given, respectively, by

$$\mathbf{R}_i^l = \sum_j \left[\left(\mathbf{u}_i^l \cdot \nabla_{ij}^l\right)\mathbf{u}_j^l + F_0^{-2}\nabla_{ij}^l h_j^l\right] + R_0^{-1}\left(z_i^l + F_i^l\right)\mathbf{x}_i^l \times \mathbf{u}_i^l + \left(\mathbf{u}_i^l \cdot \mathbf{u}_i^l\right)\mathbf{x}_i^l, \tag{28}$$

and

$$S_i^l = \sum_j \left[\mathbf{u}_i^l \cdot \nabla_{ij}^l h_j^{*l} + h_i^{*l} \nabla_{ij}^l \cdot \mathbf{u}_j^l \right]. \tag{29}$$

The spatially discretized forms of the scalar evolution equations (11)–(13) take the form

$$\frac{\partial \mathbf{W}_i^l}{\partial t} = \left(-F_0^{-2} h_i^l - \frac{1}{2} \mathbf{u}_i^l \cdot \mathbf{u}_i^l + \Lambda_i^l, T_i^l[Q], T_i^l[h^*] \right), \tag{30}$$

in which the three-component vector $\mathbf{W}_i^l$ corresponds to $(\chi_i^l, Q_i^l, h_i^{*l})$, Λ_i^l is the evaluation at position $\mathbf{x}_i^l$ of the field satisfying

$$\nabla^2 \Lambda = (Q - z - F) Q - \mathbf{x} \cdot (\mathbf{u} \times \nabla Q), \tag{31}$$

and $T_i^l[\,\cdot\,]$ generically denotes the discretization

$$T_i^l[\Phi] \equiv - \sum_j \left[\mathbf{u}_i^l \cdot \nabla_{ij}^l \Phi_j^l + \Phi_i^l (\nabla^2)_{ij}^l \chi_j^l \right]. \tag{32}$$

In Eqs. (30) and (32), $\mathbf{u}_i^l$ are determined by the discrete form of Eq. (14), namely

$$\mathbf{u}_i^l = \sum_j \left(-\mathbf{x}_i^l \times \nabla_{ij}^l \psi_j^l + \nabla_{ij}^l \chi_j^l \right). \tag{33}$$

3.3. *Laplacian Inversion*

In the solution of Eqs. (15), (18), and (31), it is required that we obtain numerical solutions to Poisson problems with right-hand sides whose values at positions $\mathbf{x}_i^l$ are ρ_i^l. In these three equations, ρ_i^l values are computed, respectively, as

$$\rho_i^l = -Q_i^l + z_i^l + F_i^l \tag{34}$$

$$\rho_i^l = - \sum_{\alpha=1}^{3} \sum_{\beta=1}^{3} \left\{ \sum_{j,k} \left(\frac{\partial}{\partial x^\alpha} \right)_{ij}^l \left(\frac{\partial}{\partial x^\beta} \right)_{ik}^l u_{\alpha j}^l u_{\beta k}^l + \sum_j u_{\alpha i}^l \left(\frac{\partial^2}{\partial x^\alpha \partial x^\beta} \right)_{ij}^l u_{\beta j}^l \right\}$$
$$- \sum_j \nabla_{ij}^l \cdot \left[(z_j^l + F_j^l) \mathbf{x}_j^l \times \mathbf{u}_j^l + (\mathbf{u}_j^l \cdot \mathbf{u}_j^l) \mathbf{x}_j^l \right] + \rho_i^{*l} \tag{35}$$

$$\rho_i^l = \left(Q_i^l - z_i^l - F_i^l \right) Q_i^l - \sum_j \mathbf{x}_i^l \cdot \left(\mathbf{u}_i^l \times \nabla_{ij}^l Q_j^l \right). \tag{36}$$

In Eq. (35), we have introduced $(u_{1i}^l, u_{2i}^l, u_{3i}^l)$ as the components of the vector $\mathbf{u}_i^l$, as well as an additional term, ρ_i^{*l}, which will be specified (see below) so as to cancel the generation of local divergence in the vector barotropic model. The matrices $(\partial/\partial x^\alpha)_{ij}^l$ and $(\partial^2/\partial x^\alpha \partial x^\beta)_{ij}^l$ may be obtained by exactly the same procedure as that employed to obtain the discrete operators ∇_{ij}^l and $(\nabla^2)_{ij}^l$ (see the previous subsection and Stuhne and Peltier [1]). However, the Poisson problem itself is *not* discretized according to this procedure. We treat it, rather,

in terms of a finite element Galerkin procedure (see, e.g., Becker *et al.* [27]), which results, at any grid level l, in the discrete equation system

$$\sum_j S^l_{i,j} \Psi^l_j = b^l_i, \tag{37}$$

in which Ψ^l_j is the solution to be obtained (ψ^l_i, h^l_i, and Λ^l_i in the respective Eqs. (15), (18), and (31)), $S^l_{i,j}$ is the finite element density matrix, and the RHS, b^l_i, is ρ^l_i, weighted by the finite element mass matrix, $M^l_{i,j}$; i.e.,

$$b^l_i \equiv \sum_j M^l_{i,j} \rho^l_j. \tag{38}$$

For the details of how $S^l_{i,j}$ and M^l_{ij} are obtained for the spherical icosahedral grid, the reader is referred to Stuhne and Peltier [1]. The only nonstandard aspect of the analysis which needs to be mentioned here is the fact that we employ the basis functions and recurrence relations which were specifically derived by Baumgardner and Frederickson [10] for this grid and which have a number of favourable numerical characteristics already discussed.

The solution of Eq. (37) is carried out by means of the multigrid algorithm of Karpik and Peltier [28] which was also specifically designed for the icosahedral grid. In Stuhne and Peltier [1] we describe and denote by `MG2DS` the implementation of a 2D version of this algorithm, the original version of which, denoted by `MG3DS`, applied to a 3D shell of finite thickness. The basic operation of the `MGxDS` multigrid algorithms invokes the simple sawtooth restriction–prolongation cycle (see Hackbusch [2]) and may be represented abstractly in the form of a recursive specification for an inverse operator for Eq. (37) which may be applied iteratively at level l:

$$\mathcal{L}^{-1,l}\{b^l_i\} = \begin{cases} \left(S^0_{i,j}\right)^{-1} b^l_j, & l = 0 \\ \mathcal{S}^l\left(b^l_i\right) \circ \mathcal{P}^{l-1} \circ \mathcal{L}^{-1,l-1} \circ \mathcal{R}^l\{b^l_i\}, & l \neq 0. \end{cases} \tag{39}$$

In the above, the restriction and prolongation operators, $\mathcal{R}^l$ and $\mathcal{P}^l$, appropriately transform the finite element representation of the RHS at level l to the respective levels $l-1$ and $l+1$. In the 2D case, the RHS-dependent operator, $\mathcal{S}^l(b^l_i)$, is the diagonal component of the line Jacobi mass lumped smoothing operator of Karpik and Peltier [28]. Its specific form, along with other details of the multigrid algorithm, is provided in Stuhne and Peltier [1].

3.4. *Time Stepping*

In Stuhne and Peltier [1] we described and compared simulations in which the time-stepping was carried out either by means of a Lax–Wendroff advection scheme on the icosahedral grid or by means of a straightforward leapfrog time-stepping scheme. The Lax–Wendroff scheme (see Lax and Wendroff [29]) invokes a special discretization of equations of the type of (1) which was found, in the barotropic model of Stuhne and Peltier [1], to exhibit a greater degree of numerical stability, but somewhat poorer energy conservation characteristics. In the case of shallow-water dynamics, the divergence equation (11) is not in flux form and must consequently be handled by some alternative means of advection. We therefore consider in this study only leapfrog time-stepping under which the temporal

discretizations of the evolution equations (27) and (30) for $\mathbf{V}_i^l$ and $\mathbf{W}_i^l$ take the generic form

$$\mathbf{A}_i^l(t+\Delta t) = \mathbf{A}_i^l(t-\Delta t) + 2\Delta t \mathbf{N}_i^l[\mathbf{A}(t)], \tag{40}$$

in which $\mathbf{A}_i^l(t)$ is the appropriate three- or four-component vector at (discrete) time t, and we define

$$\mathbf{N}_i^l[\mathbf{A}(t)] \equiv \mathbf{RHS}_i^l[\mathbf{A}(t)] + \nu \sum_{p,q,r} (\nabla^2)_{ip}^l (\nabla^2)_{pq}^l (\nabla^2)_{qr}^l \mathbf{A}_r^l(t), \tag{41}$$

where $\mathbf{RHS}_i^l[\mathbf{A}(t)]$ denotes the evaluation of the RHS of Eq. (27) or (30) at that time, and the summation term represents a numerical approximation to a ∇^6 hyperviscosity term with parametric coefficient ν. This filtering term is usually needed to suppress numerical instabilities arising from grid-scale noise and computational waves. The familiar time-splitting instability of the leapfrog scheme (see, e.g., Haltiner [30]) has been eliminated by inserting, at every tenth time step, a "restart" step of the form

$$\mathbf{A}_i^l\left(t+\frac{\Delta t}{2}\right) = \frac{1}{2}\left(\mathbf{A}_i^l(t) + \mathbf{A}_i^l(t-\Delta t)\right) + \Delta t \mathbf{N}_i^l[\mathbf{A}(t)] \tag{42}$$

$$\mathbf{A}_i^l(t+\Delta t) = \mathbf{A}_i^l(t) + \Delta t \mathbf{N}_i^l\left[\mathbf{A}\left(t+\frac{\Delta t}{2}\right)\right], \tag{43}$$

which is an Euler backward step (*op. cit.*) with an additional averaging between the t and $t-\Delta t$ time levels. These implementations of spatial and temporal filters will be seen to be adequate for purposes of this study, but they suffer from some deficiencies. The application of the high-order hyperdiffusion operator, $\nabla^6 = (\nabla^2)^3$, can itself introduce a ν-dependent restriction upon the Courant number beyond the standard CFL criterion. This is clearly not desirable, and we are investigating possible improvements, such as might be achieved with time-lagged dissipation operators (see Browning *et al.* [31]). Even as the methods currently stand, however, they are by no means unique in exhibiting such a shortcoming. For instance, Heikes and Randall [14] report a similar time step restriction tied to the occurrence of the Laplacian operator in their discretized evolution equations. Temporal filtering in our methodology could also potentially be improved with the application of alternative techniques (e.g., Asselin [32]).

Two additional points require mention in relation to the time-stepping scheme. First, the underdetermined initial conditions of the discrete equation (40) may be fully specified by taking a "restart" step of the form (42)–(43), while assuming

$$\mathbf{A}_i^l(-\Delta t) = \mathbf{A}_i^l(0) - \Delta t \mathbf{N}_i^l[\mathbf{A}(0)]. \tag{44}$$

Second, in order to inhibit the accumulation of divergence in the vector barotropic model, we set the ρ_i^{*l} term in Eq. (35) as

$$\rho_i^{*l}(t) = \begin{cases} 2\Delta t^{-1} \sum_j \nabla_{ij}^l \cdot \mathbf{u}_j^l(0), & \text{if } t = 0, \\ \Delta t^{-1} \sum_j \nabla_{ij}^l \cdot \mathbf{u}_j^l\left(t - \frac{\Delta t}{2}\right), & \text{if } t = \left(10M + \frac{1}{2}\right)\Delta t, \\ (2\Delta t)^{-1} \sum_j \left(\nabla_{ij}^l \cdot \mathbf{u}_j^l(t) + \nabla_{ij}^l \cdot \mathbf{u}_j^l(t-\Delta t)\right), & \text{if } t = 10(M+1)\Delta t, \\ (2\Delta t)^{-1} \sum_j \nabla_{ij}^l \cdot \mathbf{u}_j^l(t-\Delta t), & \text{otherwise,} \end{cases} \tag{45}$$

in which $M \geq 0$ is an integer.

3.5. *Surface Integrals and Invariants*

In the analysis of the test cases of Williamson *et al.* [11] and for the purpose of other tests, it is necessary to estimate global surface integrals of the form

$$I(h) = \frac{1}{4\pi} \int_0^{2\pi} \int_{-\pi/2}^{\pi/2} h(\lambda, \theta) \cos\theta \, d\theta \, d\lambda \tag{46}$$

(in which we use the symbols of Williamson *et al.* [11]). We have found, for the case of our numerical methodology, that good results are efficiently obtained if we estimate such integrals as simple averages over points on a given grid level l; i.e.,

$$I(h) \approx \frac{1}{10n^2 + 2} \sum_i h_i^l, \tag{47}$$

where, as before, $n = 2^l$. The accuracy of this estimate is only weakly compromised by the slight differences between the areas of individual spherical polygonal cells that exist at a given level of resolution.

Three important positive-definite global invariants of the shallow water dynamical system are the surface integrals of h^* (mass), $\frac{1}{2}h^*\mathbf{u} \cdot \mathbf{u} + (h^2 - h_s^2)/(2F_0^2)$ (total energy), and $Q^2/(2h^*)$ (potential enstrophy). The corresponding barotropic values for total energy and potential enstrophy are simply the surface integrals of $\frac{1}{2}\mathbf{u} \cdot \mathbf{u}$ and $\frac{1}{2}Q^2$, respectively. For these invariants, one defines normalized "conservation-violations" at time t as

$$I_i(\xi(t)) = \frac{I(\xi(\mathbf{x}, t)) - I(\xi(\mathbf{x}, 0))}{I(\xi(\mathbf{x}, 0))} \tag{48}$$

(see Williamson *et al.* [11]).

For the test cases of Williamson *et al.* [11], comparison must be made with analytical solutions of the shallow-water equations expressed in terms of the three fields $h_T(\lambda, \theta, t)$, $u_T(\lambda, \theta, t)$, and $v_T(\lambda, \theta, t)$ where the latter two are the 2D velocity components in the spherical polar coordinate basis. Using the definitions of Williamson *et al.* [11], it is a simple matter to compute the l_1, l_2, and l_∞ errors in the h and $\mathbf{u}$ fields predicted by our icosahedral model if we define, at position $\mathbf{x}_i^l$, the fields:

$$u = \frac{\left(\mathbf{e}_z \times \mathbf{x}_i^l\right) \cdot \mathbf{u}_i^l}{\left(x_i^l\right)^2 + \left(y_i^l\right)^2} \tag{49}$$

$$v = \frac{\left[\mathbf{e}_z - \mathbf{x}_i^l\left(\mathbf{e}_z \cdot \mathbf{x}_i^l\right)\right] \cdot \mathbf{u}_i^l}{\left(x_i^l\right)^2 + \left(y_i^l\right)^2}. \tag{50}$$

The contribution to the error of the north and south polar points is taken to be zero since the basis vectors may be chosen arbitrarily there.

3.6. *Nomenclature*

For brevity in what follows, we will introduce a simple convention for naming the various numerical models which result from the discretizations outlined in this section. Barotropic models will be referred to as $x$bt$l$, in which l is the grid level number and x is v for a vector

model and s for a scalar model. Shallow water models are given names of the form *x*sw*l*, in which *l* and *x* play the same roles. A few examples will suffice to convey the meaning: sbr6 is a scalar barotropic model at grid level 6 (as in most of the simulations of Stuhne and Peltier [1]); ssw5 is a scalar shallow model on a level-5 grid; vsw7 is a vector shallow model on a level-7 grid, etc.

4. TEST CASES I: THE STANDARD TEST SUITE

The first results which we will consider, that have been obtained by applying the methodology outlined in the preceding section, derive from the standard numerical tests proposed by Williamson *et al.* [11] for shallow-water models on the sphere. In performing these tests, we have utilized a variety of subroutines and data which were obtained from the /pub/chammp/shallow directory of the ftp.cgd.ucar.edu server. First, all evaluations of analytically specified fields were performed with the original components of the CHAMMP semispectral shallow-water model on a 640×320 Gaussian grid. Results were then bilinearly interpolated onto the appropriate icosahedral grids. This is probably slightly less accurate than direct evaluation at grid points, but we have found that interpolation errors are extremely small. The same method was employed to evaluate fields from netCDF files containing observational data since we found that the routines supplied for the evaluation of spectral fields at arbitrary points were both prohibitively inefficient and less accurate at grid levels 6 and 7. Finally, we also employed the CHAMMP model routines for plotting contoured data and errors after interpolating linearly from the geodesic triangles of the icosahedral grid to the points of the Gaussian grid.

All of the standard tests of Williamson *et al.* [11] have been carried out in 32-bit arithmetic on an SGI Challenge L server employing vsw*l* models. In order to make additional comparisons, a number of these simulations were also reproduced with ssw*l* models or by using 64-bit arithmetic on a Cray J90. The standard bases for comparison are the published solutions of Jakob-Chien *et al.* [33] for the spectral transform model. None of the icosahedral grid point models discussed (our own included) has yet achieved matching accuracy in the dynamical tests. Amongst the other numerical methodologies referred to, the most recent, and the one most comparable with ours, is that of Heikes and Randall [14, 15]. In particular, the twig02562 and twig10242 models of these authors, which were integrated in ($\geq$64-bit) Cray arithmetic, have the same number of degrees of freedom, respectively, as ssw4 and ssw5 models. In the selection of results to be discussed herein, we will make a number of comparative references to Heikes and Randall [14, 15] and it will be of benefit to consider two general points at the outset. First and trivially, some of the plots in the above-cited papers deviate from the formats requested in Williamson *et al.* [11], e.g., in showing different projections and illustrating contours of $h_T - h$ rather than $h - h_T$ as the error from reference solution h_T. As already stated, we have employed the original plotting routines and conventions. The second point, which is of far greater significance, is the attention given by Heikes and Randall [15] to the issue of the global accuracy of numerical operators on their twisted icosahedral grid. Specifically, they have shown, in considering the analogues of our grid levels 2 through 5, that their finite difference discretization manifests a degradation of accuracy which makes the operators significantly less than second-order accurate over higher resolution ranges. Heikes and Randall [15] describe a modification of the basic grid structure which allows for the difficulty to be controlled in the case of the discretized Laplace and flux-divergence operators, but it remains a problem for the other

operators (in particular, they do not consider the effects of making multiple passes through the data in computing the $\nabla^2(\mathbf{u}^2/2)$ operator). The finite element multigrid methods and numerical differential operators described in Section 3 and in Stuhne and Peltier [1] are derived in a way which circumvents the *a priori* difficulties associated with the techniques that Heikes and Randall adapt from Williamson [8] and Masuda and Ohnishi [13]. However, in discussing the practical application of our methods to Test Case 3 below, we will illustrate that there is nevertheless a marked degradation of the convergence rate on high resolution grids ($l = 6$ and $l = 7$) which can be attributed to a number of factors. It should therefore not be assumed that the issue of operator convergence has necessarily been fully resolved for icosahedral grid structures in the present work and this is an area which therefore warrants further study. We do not analyze it in detail herein, nor do we attempt to implement optimizations of our numerical methodology. Our focus, rather, will be on the numerical issues previously discussed.

Space will not permit us to discuss herein the results obtained for all of the standard tests of Williamson *et al.* [11]. In particular, Test Cases 4 and 6 will not be analyzed and we will not deal with Test Case 1, except to simply note that a similar advection test for the Lax–Wendroff scheme on our grid was described in Stuhne and Peltier [1]. The results obtained for the standard advection test under the leapfrog integration scheme employed in this study manifest an error distribution and magnitude that are very similar to those reported by Heikes and Randall [14] for the corresponding resolution using their methodology.

4.1. *Test Case 2: Global Steady-State Nonlinear Balanced Flow*

The first test case we will consider assumes an initial Q_0 field that represents a simple solid body rotation and takes the form

$$Q_0 = \frac{13}{12} z', \tag{51}$$

in which z' is a coordinate whose axis is the original z-axis rotated by an angle α towards the original x-axis; i.e.,

$$z' = z \cos\alpha + x \sin\alpha. \tag{52}$$

If we take the new Coriolis parameter to be z' (rather than z) and set h_0 to the balanced height field corresponding to this nondivergent flow, then we have, for any rotation angle α, a steady state flow which should remain unchanged for all time. Errors and imperfections in the numerical solution may be ascertained by comparison with the analytical solutions for u, v, and h provided in Williamson *et al.* [11]. All simulations to which we refer herein have been integrated for the required 5 days at grid level five with a time step $\Delta t = 225$ s and a (dimensional) diffusion parameter $\nu = 6.4 \times 10^{25}$ m^6/s. Like Heikes and Randall [14], we have found that the quality of the solutions does not appreciably depend upon the rotation angle α, verifying that our grid and discretization are almost spatially homogeneous in the way in which they resolve the surface of the sphere.

In Fig. 2, we plot the l_∞ error in h as a function of time for four integrations: specifically, a 32-bit and a 64-bit run with each of the models `vsw5` and `ssw5` at rotation angle $\alpha = \pi/2$. What this figure clearly shows is that the approximate steady-state height field in the `vsw5` simulations fluctuates little, in the l_∞ sense, from the initial estimate obtained by solving the

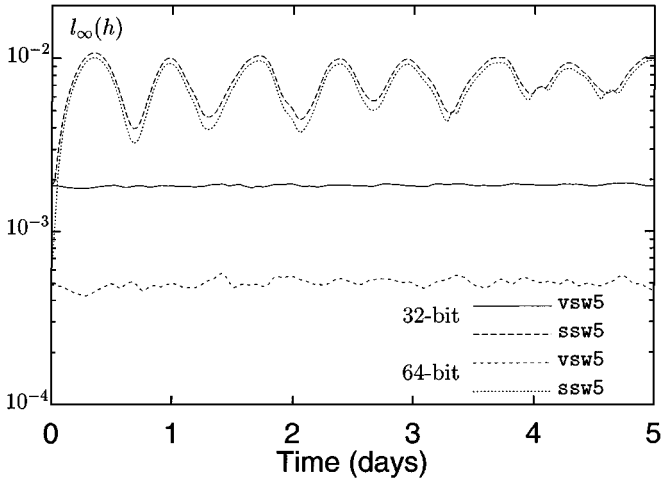

FIG. 2. Test Case 2. Time series of $l_\infty(h)$ errors for 32-bit and 64-bit integrations of `vsw5` and `ssw5` models for steady state solid-body rotation with $\alpha = \pi/2$.

discrete form of Eq. (17) (in which we choose H_0 so that the constant component agrees with that in the analytical solution of Williamson *et al.* [11]). As might be expected, the $l_\infty(h)$ error is appreciably (about four times) smaller, where this elliptic Poisson problem is solved at higher numerical precision. The error in the 64-bit `vsw5` simulation is about 4.5×10^{-4}, as compared to the $l_\infty(h)$ error of approximately 1.5×10^{-4} manifested by Heikes' and Randall's [14] `twig10242` model for this same case. Given the clearly sensitive dependence of the error measures upon numerical precision, the modest discrepancy could easily be accounted for in terms of factors already discussed (in particular, the special optimizations applied by Heikes and Randall to the discrete Poisson problem as well as our method of interpolating analytical fields). If this is taken into consideration, it is fairly safe to conclude that the performance of our `vsw5` model is quite comparable to that of Heikes and Randall's [14, 15] `twig10242` model. This is, however, *not* the case with our `ssw5` model, in which, as Fig. 2 shows, the $l_\infty(h)$ error quickly rises to and then fluctuates over a range of substantial values (5×10^{-3}–10^{-2}). Furthermore, except in the very early stages of the integration, the character of this error is *not* sensitive to numerical precision in the sense that the 32-bit and the 64-bit results do not differ appreciably. We therefore see that the quality of steady-state solutions is significantly poorer under `ssw5` integrations, but it is more stable with respect to small computational inaccuracies.

It is interesting to note the fact that Heikes' and Randall's [14, 15] `twig10242` model, which incorporates only scalar quantities as integrated prognostic variables, has performance similar to our vector `vsw5` model. Our own scalar `ssw5` model, in contrast, manifests an initial transient and converges to a computational steady state slightly different from the imposed *a priori* analytical flow. Another way of saying this is that the numerical state of "balance" for the discrete form of system (11)–(13) appears, due to the particular sequence of operations implicit in its solution, not to coincide precisely with the Charney [26] balance criterion of Eq. (17). There is, however, no *a priori* problem in this since the definition of Charney balance itself derives from somewhat arbitrary approximations. As we shall see in the results of Case 5 below, there is little discrepancy between the error norms of `vsw5` and `ssw5` simulations under non-steady-state conditions.

4.2. *Test Case 3: Steady-State Nonlinear Balanced Flow with Compact Support*

This test case is identical to Case 2, except that the Q_0 initial condition in the rotated coordinate system represents a more complex flow, containing a compact zonal jet within a limited range of (rotated) latitudes and a vanishing velocity field outside this region (see Williamson *et al.* [11]). At given resolution, we have employed the same numerical parameters in these integrations as in Case 2. Specifically, we employ, at grid level l, a time step $\Delta t = 2^{5-l}\Delta t_0$, and a hyperdiffusive filtering parameter $\nu = 32^{5-l}\nu_0$, where Δt_0 and ν_0 are the level-5 values given in the preceding subsection.

Appropriate comments in connection with the results obtained from our simulations of Case 3 are generally the same as those for Case 2. As previously stated, we will consider the convergence properties of the l_1, l_2, and l_∞ errors in h and $\mathbf{u}$ after 5 days with increasing grid level l. Results are shown in Fig. 3 from 32-bit `vsw`l integrations for $\alpha = \pi/3$ and l varying from 3 to 7. We plot, in addition to the six basic error measures, the curve $(0.8 \times 2^{-l})^2$, whose functional form indicates an ideal quadratic convergence rate with respect to the mesh constant. It is thereby shown that this theoretically expected convergence rate is closely maintained up to level 5 by all error measures and up to level 6 by all but the $l_\infty(\mathbf{u})$ error (which can be somewhat quirky when a few grid points fall very close to the poles of the imposed spherical polar coordinate system). Between levels 6 and 7, however, there is a clear degradation in the convergence properties of all error measures. As we have already discussed, it is a significant issue as to whether or not this and similar results are symptomatic of a general convergence problem similar to that discussed by Heikes and Randall [15]. In considering this possibility, it should be noted, however, that the errors in these results from Case 3 include the combined contributions of spatial and temporal truncation errors, computational noise, numerical imprecision, interpolation, and other factors which have not

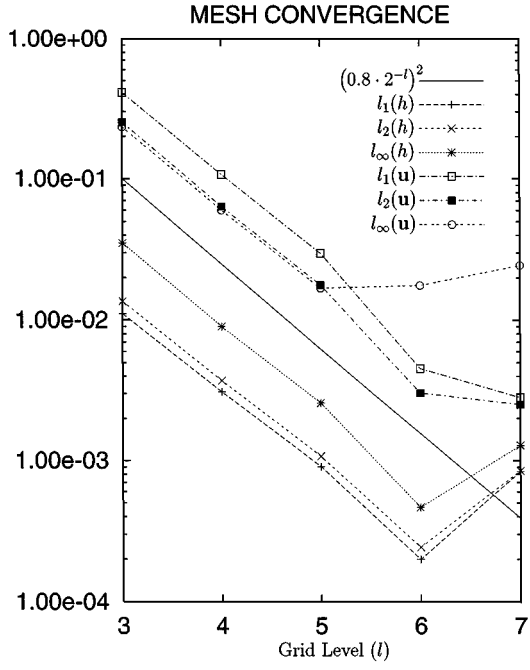

FIG. 3. Test Case 3. Convergence with grid level, l, of l_1, l_2, and l_∞ error norms of h and $\mathbf{u}$ after 5 model days.

been considered in a controlled way. We have not, as yet, developed any means of precisely quantifying these various influences at very high grid-point resolution, nor could we find any published results pertaining to comparably fine icosahedral mesh structures. Over the range of resolutions which are commonly considered, the convergence properties of our model are very good.

4.3. *Test Case 5: Zonal Flow over an Isolated Mountain*

The initial condition for this case is specified identically to that of Case 2, except for the choice of $\alpha = 0$ (i.e., $z' = z$), of a slower solid body rotation field described by

$$Q_0 = 1.043049z, \tag{53}$$

and of a nonzero static underlying topography given by

$$h_s = \frac{50}{149}\left\{1 - \min\left[1, \frac{9}{\pi}\sqrt{\left(\lambda - \frac{3\pi}{2}\right)^2 + \left(\theta - \frac{\pi}{6}\right)^2}\right]\right\}. \tag{54}$$

This choice of the h_s field corresponds to an isolated mountain of nondimensional height $50/149$ (about $1/3$ of the total fluid layer thickness) which is centered at polar coordinates $(\lambda_c, \theta_c) = (3\pi/2, \pi/6)$ (see Williamson *et al.* [11]). Such a feature plays a role similar to that of the quasi-topographic forcing, F, introduced in our vortex erosion simulations (next section). Namely, it is a spatially fixed anomaly which excites strong nonlinear waves in the steady basic state. In the present case, however, the configuration does not result in an intense enstrophy cascade with its associated chaotic vortex dynamics. The flow is, therefore, considerably simpler from a computational perspective.

No analytical solution is available for the unsteady flow that develops in Case 5, so comparisons may only be made at 1-day intervals with results output from a high resolution T-213 semispectral model and distributed in the file `REF0114.cdf`. We have performed 32-bit integrations of this case over the required 15-day interval with both `vsw5` and `ssw5` models employing (dimensional) numerical parameter values $\nu = 5.12 \times 10^{26}$ m^6/s and $\Delta t = 56.25$ s. In Fig. 4, we show contour plots after 15 days of the `vsw5` height field, h, and of the deviation, $h - h_T$, from the T-213 simulation for both the `vsw5` and the `ssw5` integrations. The h contour plot is virtually indistinguishable by inspection from the `twig10242` results illustrated by Heikes and Randall [14]. Furthermore, the `vsw5` error field shows a very similar distribution to that of the `twig10242` and `twig02562` models of these authors, although the absolute magnitudes of the errors are slightly smaller in the $\geq$64-bit `twig10242` results and slightly larger in the corresponding results from `twig02562` (whose resolution corresponds to our grid level 4). Examination of the error field for the `ssw5` model in Fig. 4 reveals that the magnitudes of the error in the contoured field do not differ significantly from those in the `vsw5` results, but that the spatial distributions do differ somewhat. The fact that these integrations quickly approach a stage in which the quantitative error measures are very similar is confirmed in Fig. 5, in which we plot time series of the l_1, l_2, and l_∞ errors of h for both `vsw5` and `ssw5` models. The discrepancy in the spatial distribution of errors is explicable in terms of our earlier remark that the discrete forms of the two mathematical formulations appear to embody slightly different criteria of balance (or, in the terminology introduced by Leith [34], slightly different "slow manifolds").

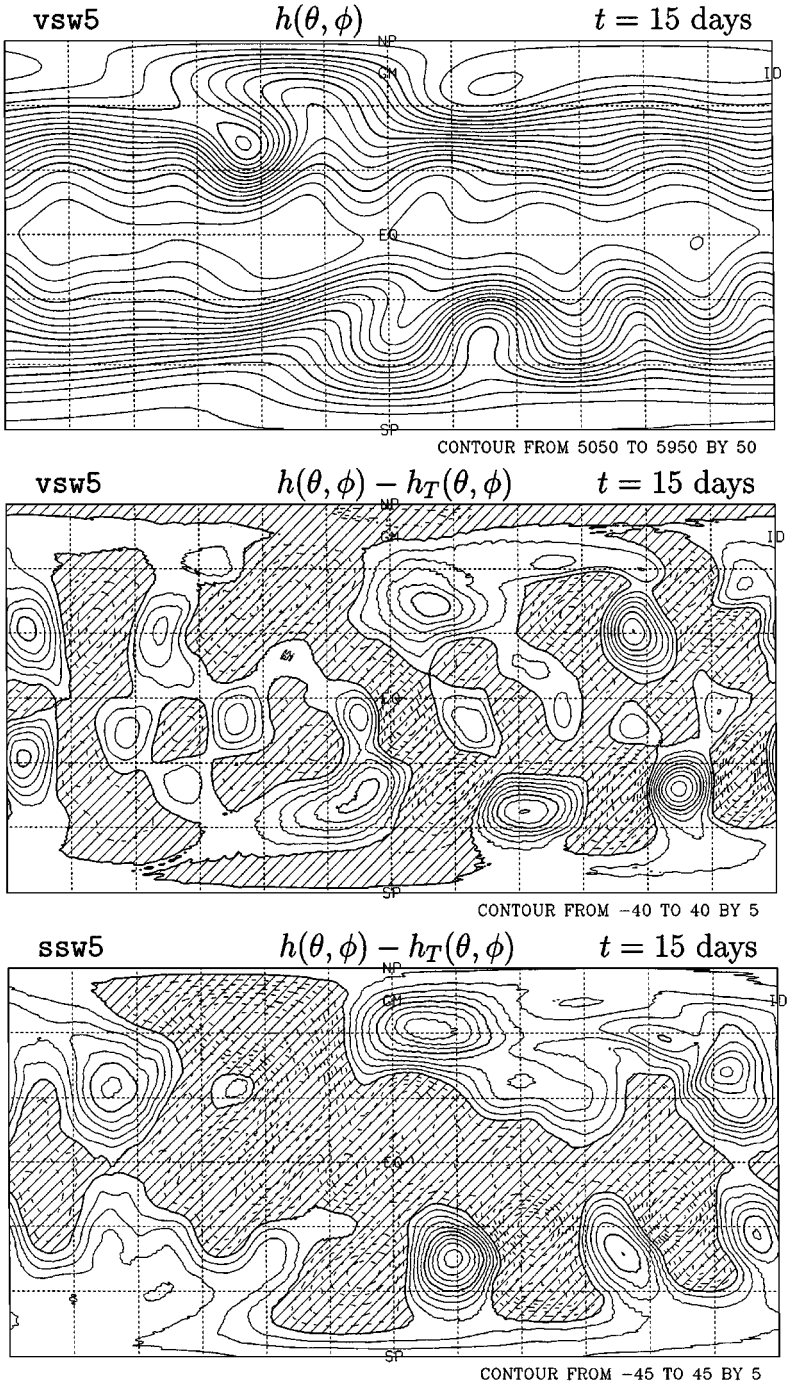

FIG. 4. Test Case 5. Height field, h, of `vsw5` model after 15 days and corresponding deviation, $h - h_T$, from high-resolution T-213 simulation for `vsw5` and `ssw5` models.

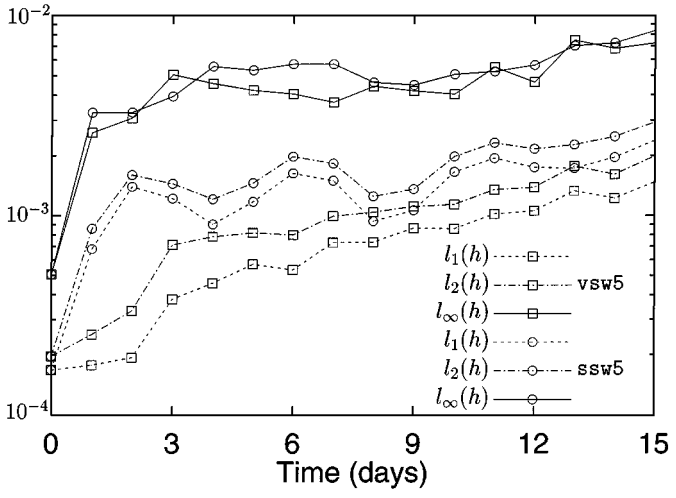

FIG. 5. Test Case 5. Time series of l_1, l_2, and l_∞ error norms of h for `vsw6` and `ssw6` simulations.

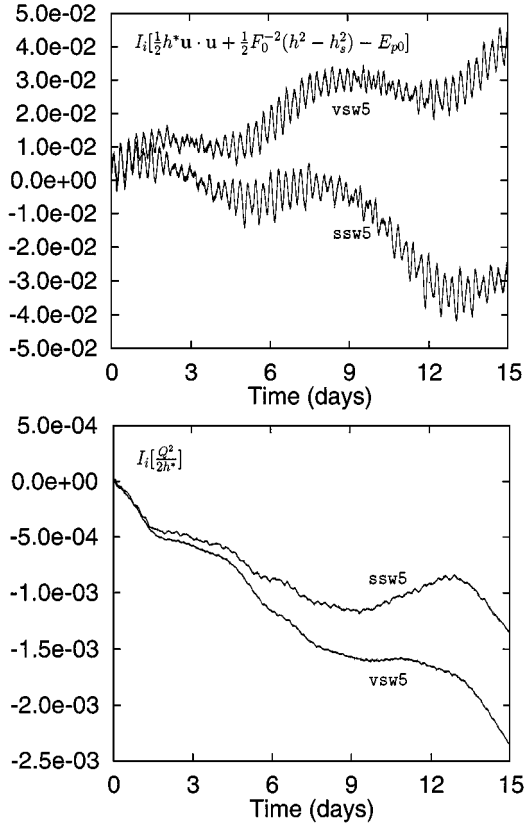

FIG. 6. Test Case 5. Shallow-water total energy and potential enstrophy conservation results for `vsw6` and `ssw6` simulations.

To complete our consideration of Case 5, we turn our attention to Fig. 6, which shows time series of the fractional conservation violations, $I_i(\xi)$, in the total numerical shallow-water energy and potential enstrophy of the `vsw5` and `ssw5` models. In order to deemphasize the influence on the total energy of the large background height field, we follow Heikes and Randall [14] in subtracting the potential energy, E_{p0}, of a reference state (we employ the solution at $t = 0$ for this purpose). The conservation properties for $E - E_{p0}$ of our two models are essentially identical in terms of the maximum global violations (about 0.04), but they do differ somewhat in the detailed time evolutions of this error after the very early stages of the simulation. The results of both, in the sense of absolute fractional deviations, are very similar to those reported by Heikes and Randall [14] for their models (about 0.05). The potential enstrophy conservation of the `twig10242` model of Heikes and Randall [14], in contrast, is better than that of either of our models, manifesting a deviation of about 2×10^{-5} over the run. Our potential enstrophy conservation violations are, for comparison, about 1×10^{-3} for `ssw5` and 2×10^{-3} for `vsw5`. These violations are manifested in the decay of enstrophy, as would be physically reasonable on the basis of dissipation by subgrid scale processes. Interestingly, Heikes' and Randall's [14] enstrophy violations, although quantitatively smaller, appear as an unnatural *enhancement* of this quantity which could prove destabilizing in strongly nonlinear simulations (such as the vortex erosion tests which we consider in the next section), wherein there is a very intense nonlinear enstrophy cascade taking place.

It is not surprising that models which explicitly discretize the conservation law of flux form governing Q should exhibit better global enstrophy conservation properties, as occurs in the relation between our `ssw5` and `vsw5` results. Heikes' and Randall's models, in which the time-stepping scheme for h^* and Q is constructed explicitly on the basis of the flux-conservation laws, exhibit still better global enstrophy conservation. Flux-conserving advection schemes are easily incorporated into our own scalar models and, indeed, we have already experimented with a simple Lax–Wendroff method (see Stuhne and Peltier [1]). In the present study, we have avoided introducing such complicating factors and consider only direct local approximations of the governing PDEs.

4.4. *Test Case 7: Prescribed Height and Velocity Initial Conditions*

The last standard test case for shallow-water models on the sphere that we will describe entails the direct initialization of a numerical integration with, in general, a divergent velocity field derived from atmospheric observations, along with a height field which is defined so as to correspond to the measured altitude of the 500-mb pressure surface in these observations. We will consider herein only the particular subcase in the test suite which is initialized with the atmospheric data of 00:00 GMT on Dec. 21, 1978 (see Williamson *et al.* [11]). These initial conditions (to which nonlinear normal mode initialization has been applied so as to reduce spurious gravity wave activity) are, along with the output at days 1, 2, 3, 4, and 5 from a subsequent high-resolution (T-213) spectral transform integration, distributed in the file `REF0077.cdf`. We set $\mathbf{u}_0$ and h_0 in an `vsw5` model according to these initial conditions and integrate for 5 days with the same ν and Δt parameters employed in Case 5. Figure 7 presents, in the form of two contour plots after 5 model days on a polar stereographic projection of the northern hemisphere, the height field, h, and the deviation, $h - h_T$, from the T-213 results. Once again, there is a very close correspondence between the height

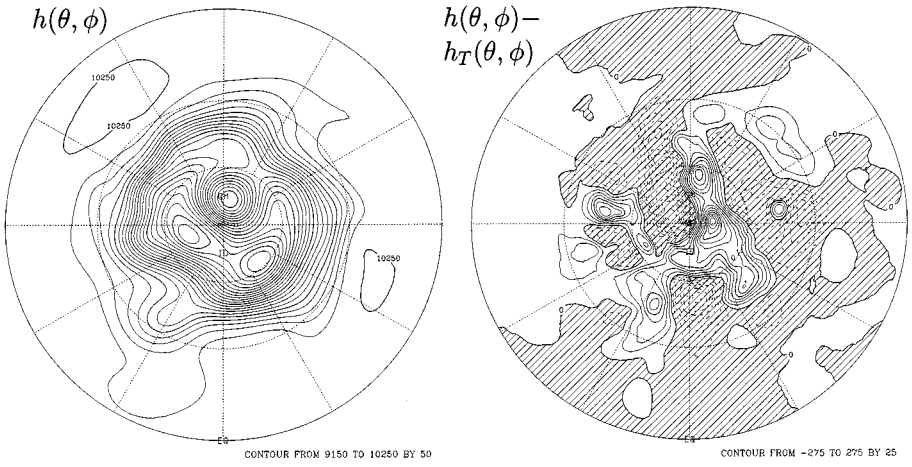

FIG. 7. Test Case 7. Height field, h, of `vsw5` model in polar stereographic projection after 5 days and corresponding deviation, $h - h_T$, from high-resolution T-213 simulation.

field of our `vsw5` simulation and that of Heikes' and Randall's [14] `twig10242` model. The height errors delivered by the two models also manifest a very similar distribution, although, in this case, it is our model which exhibits a modestly smaller error magnitude. The latter result, which is confirmed by the $l_\infty(h)$ error measures (not shown), further supports the contention, often repeated in this section, that the `vsw5` model is closely comparable in accuracy to `twig10242`, the modest discrepancies between them depending upon the detailed characteristics of the particular circumstance selected as the basis for comparison.

5. TEST CASES II: POLAR VORTEX EROSION

We next turn our attention to additional, more computationally challenging, test cases which relate to an interesting phenomenon of nonlinear wave/mean-flow interaction which occurs when a polar vortex is eroded by a quasi-steady wavenumber 1 forcing in the form of an impinging Rossby wave. The ensuing dynamical interaction, originally studied in the well-known simulations of Juckes and McIntyre [4], occurs in response to a large scale, nonzonal perturbation to the Coriolis parameter that is smoothly activated and then deactivated over a period of many model days. Juckes and McIntyre [4] have demonstrated, in the course of their work which employed a spectral transform, absolute vorticity advecting discretization of the nondivergent barotropic governing equations, that this forcing induces a nonlinear wave-breaking event at a latitude where the zonal phase speed of the wave matches the zonal velocity of the mean flow, which culminates in the erosion of small-scale vortices and thin vorticity filaments from the main polar vortex. The secondary vortical structures thereafter interact with each other and with the zonal flow in a way that closely mimics the atmospheric phenomenon that occurs in the wintertime stratosphere of Earth's southern hemisphere, a phenomenon that is of considerable importance to the understanding of the Antarctic ozone hole.

We will not concern ourselves further herein with discussion of the physics of the vortex erosion problem since this has been extensively discussed elsewhere. Following the

arguments presented in Stuhne and Peltier [1], we will, rather, employ this phenomenology to define an especially challenging benchmark that may be used to further investigate the quality of numerical models of flow on the 2-sphere. As such, it is particularly useful from the perspective of the present study since, unlike the previously discussed tests of Williamson *et al.* [11], it is realizable within all four of our discretizations (i.e., `vbr`l, `sbr`l, `vsw`l, and `ssw`l), shallow water simulations requiring only the additional input of a Froude number, F_0. In Stuhne and Peltier [1], we have already presented and compared vortex erosion results obtained from `sbr6` models under a variety of numerical conditions and from one `sbr7` model. These simulations have verified that the dynamical processes involved in vortex erosion are properly resolved and that, moreover, their physical characteristics are essentially unaffected by variations in grid-scale numerical behaviour associated with a change of advection scheme, a change of hyperviscous diffusion parameter, or a doubling of resolution (provided, of course, that the model is numerically stable under the requisite conditions). In the present study, we set these specifics in a consistent way and focus instead upon the potentially far more significant impact of employing completely different mathematical formulations of the dynamical equations. As touched upon in the discussion of results for Test Cases 3 and 5, different discretizations of the shallow water equations can imply slight variations in the computational "slow manifold." Where this is the case, the influence of fluctuations in models with numerically identical initial conditions need *not* be confined to small-scale computational noise. Rather, in instances of chaotic flow characterized by a strong inverse energy cascade, as occurs in the later stages of polar vortex erosion, fluctuations can develop into significant deviations in the dynamically significant behaviour.

All of the simulations to be discussed have been performed with the leapfrog advection scheme on grid $l = 6$. Having approximately 320 points along any diameter, this grid level is comparable in resolution at the equator to the T-159 spectral transform model of Juckes and McIntyre [4]. In Stuhne and Peltier [1], we describe results from the `ssw6` model which are qualitatively appropriate and consistent under various changes in model parameter, but which manifest traces of anomalous, nonisotropic noise associated with thin filaments of vorticity (see Stuhne and Peltier [1]). It will be of particular interest, therefore, to examine how these and other subtle qualitative features of the small scale, nonlinear vortical structures are affected by the choice of mathematical formulation. To provide an initial point of reference, we illustrate in Fig. 8 the results of a complete 17-day integration of the vortex erosion problem obtained with our nondivergent vector barotropic model, `vbr6`. As in the `sbr6` simulations first discussed in Stuhne and Peltier [1], a (dimensional) time step of $\Delta t = 300$ s and a hyperviscosity of $\nu = 6.8 \times 10^{23}$ m^6/s were employed, the same values originally used by Juckes and McIntyre [4]. We show, at 1-day intervals, a stereographically projected, 200×200 pixellated rendition of absolute vorticity, Q, in which the intensity of each pixel is set according to the linearly interpolated value of the field at its projected center point on the surface of the sphere (the Q-scale being indicated by the colour bar). Up until approximately $t = 7$, comparison of the dynamic progression shown in Fig. 8 with the results for the `sbr6` model shown in Stuhne and Peltier [1] will reveal the two to be essentially indistinguishable. These are the stages of the evolution in which the linear and nonlinear Rossby wave-breaking dynamics commence, leading to the initial stages of filamentation evident in the $t = 7$ frame. However, as we illustrate below, once the strongly nonlinear dynamics progress beyond this critical stage, the slightly different representations of the computational "slow manifold"

implicit in the different models cause the results to begin to manifest markedly divergent features.

In order to facilitate the detailed intercomparison of the results delivered by the various models, we show, in Fig. 9, three frames at times $t = 9$, $t = 12$, and $t = 15$ from the strongly nonlinear stages of each of five different simulations. The first set is from `vbr6` (a direct reproduction from Fig. 8); the second set is from `sbr6` (a direct reproduction from Stuhne and Peltier [1]); the third and fourth sets of three frames are from the shallow-water models `vsw6` and `ssw6` integrated with $\Delta t = 20$ s and $\nu = 1.02 \times 10^{25}$ m^6/s at Froude number $F_0 = 1.48$, while the last set is from `vsw6` under the same conditions, but with $F_0 = 3.32$. In the shallow water simulations, we choose the H_0 parameter in Eq. (17) so that the mean component of the initial height field is unity, thus making the height scaling consistent with the choice of a value for H in the specification of the Froude number. As the figure confirms, the shallow water simulations with the relatively small Froude number, $F_0 = 1.48$ (corresponding to a deep layer) are in a quasi-barotropic scaling regime in which their dynamics resemble those of the nondivergent barotropic model. The similarities of phenomenology between the flows are explicable in terms of the fact that the shallow-water models should tend to persist in a "balanced" state (or, in Leith's [34] terms, on a "slow manifold") satisfying the Charney balance condition of Eq. (17) or some refinement thereof (see, e.g., McIntyre and Norton [35]). The fact that our models exhibit these similarities is further evidence of their consistency. The evident differences in the quantitative predictions of the models after the onset of Rossby wave breaking are, moreover, also explicable because any small errors in the instantaneous applicability of the balance constraints (as must arise from discretization and from the nonzero F_0 value in the shallow water simulations) will result in a chaotic amplification of deviations between trajectories beginning from the same initial condition. In order to illustrate also a case in which a large deviation from Charney balance develops and plays an important rôle in the dynamics, we also include results from the simulation at higher Froude number, $F_0 = 3.32$, wherein it is clear, as we discuss further below, that significantly different phenomenology occurs.

Examination of the $t = 9$ frame in each of the first four simulations shown in Fig. 9 will reveal that there is just beginning to be a qualitative divergence between the structures of the predicted Q fields. Specifically, the "tail" of the vorticity filament manifests varying behaviour in its interaction with the background flow; i.e., it points in different directions in the `vbr6` and `sbr6` simulations and "fades out" in the `vsw6` simulation. Also, the protuberance which is evident on the main vortex exhibits small variations of shape across the simulations. Discrepancies become considerably more pronounced in the $t = 12$ and $t = 15$ frames, with significant variations between the patterns of vortical and filamentary structures which are shown for the different simulations. All, however, manifest the appropriate qualitative behaviour and there are, moreover, significant robust features. Examples of the latter are the coherence and basic shape of the central vortex and, at time $t = 15$, the presence of a small, compact cyclone at a consistent position and of a more diffuse anti-cyclonic structure adjacent to the main vortex. One feature to note is the fact that only the `sbr6` simulation appears to manifest a significant level of what is clearly anisotropic computational noise associated with the filaments in frames $t = 12$ and $t = 15$ (the `vbr6` model shows traces at $t = 12$ but these are much fainter). The effects which we ascribed to under-resolution in Stuhne and Peltier [1] do not seem to occur appreciably in the new formulations introduced in this study.

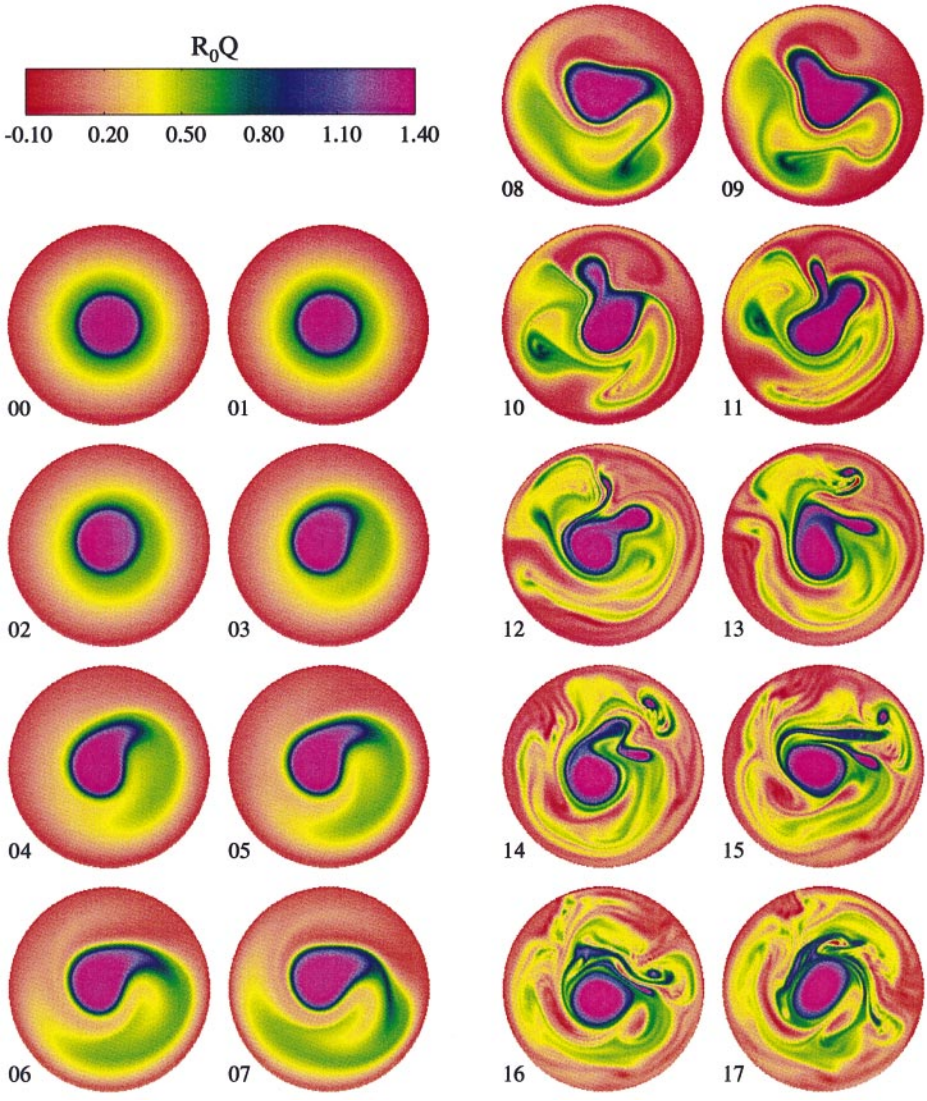

FIG. 8. Half-toned plots of the absolute vorticity field, Q, in polar stereographic projection for a `vbr6` vortex erosion simulation.

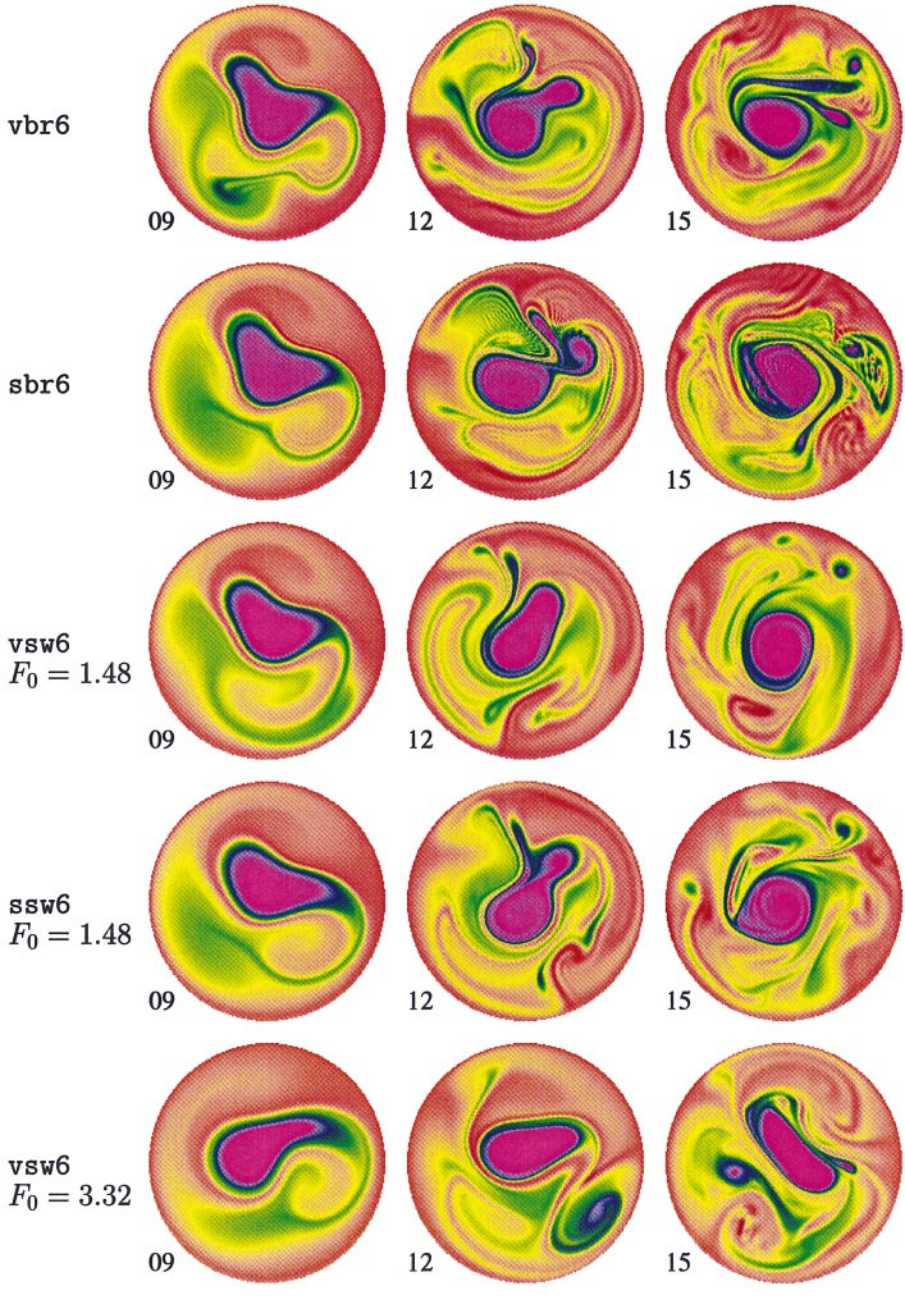

FIG. 9. Half-toned plots of the Q field at times $t = 9$, $t = 12$, and $t = 15$ for `vbr6` and `sbr6` models; `vsw6` and `ssw6` models at $F_0 = 1.48$; and `vsw6` model at $F_0 = 3.32$. Format and scaling are as in Fig. 8.

Since the basic numerical elements employed are the same, we can speculate that models with a greater number of computational degrees of freedom may be less susceptible to noise (the scalar barotropic model, of course, advects only a single prognostic scalar field).

Turning our attention, now, to the final shallow-water simulation at $F_0 = 3.32$, it will be clear that, in this regime, the pattern of the flow differs in significant ways from the nondivergent barotropic predictions. By $t = 9$, for instance, the structure formed by the polar vortex and its associated filament is shifted in phase and significantly distorted in shape from the pattern in the first four simulations. Even more pronounced discrepancies are evident at $t = 12$, where there is a clear intrusion of low absolute vorticity fluid into a narrow band around the central vortex, an effect which strongly steepens the Q gradient in this region. Similar dynamics are discussed by Juckes [36] in relation to spectral transform shallow-water simulations of the winter stratosphere under equivalent scaling conditions (although these simulations introduce forcing in a different manner and therefore cannot be directly compared to our own). Another observation to be made is that the filamentary structures in the $F_0 = 3.32$ simulation are, at later times, considerably weaker than in the $F_0 = 1.48$ and nondivergent barotropic simulations, with correspondingly more absolute vorticity concentrated in large-scale "rolled-up" structures consisting of tongues of vorticity spiralling into central "beads". Finally, as is evident in the $t = 15$ frame, the central cyclonic polar vortex in the high Froude number simulation is significantly elongated, whereas those in the other cases are close to circular. We will not discuss further herein the qualitative differences between barotropic and shallow-water results. The point which has been made is that the differing behaviour at $F_0 = 3.32$ demonstrates that our model resolves an inherently shallow-water scaling regime to which nondivergent barotropic theory is no longer a good approximation. As is to be expected, varying F_0 through a range of intermediate values (not shown) creates a continuous transition in the nature of the dynamics.

The final issue we will consider concerning the results obtained on the basis of the test simulations of the vortex erosion case pertains to the conservation of invariants by the nondivergent barotropic models `vbr6` and `sbr6`. The quasi-topographic forcing is introduced through the function F in a way which does not invalidate the formal energy and enstrophy conservation properties of the nondivergent barotropic equations and we may therefore gauge our models' performance in numerically conserving these quantities. Figure 10 shows time series of fractional conservation violations, $I_i[\frac{1}{2}\mathbf{u} \cdot \mathbf{u}]$ and $I_i[\frac{1}{2}Q^2]$, for `vbr6` and `sbr6`. These demonstrate the fact that the vector model conserves kinetic energy somewhat better than its scalar counterpart, although, in absolute terms, the variation of several percentages which occurs in each is quite large. The enstrophy conservation results tell a similar story, although, in this case it is the scalar model which performs modestly better, which is consistent with our considerations in the discussion of Test Case 5. Neither these relatively poor conservation results nor the discrepancies between the models are surprising when one recognizes, in the light of the above discussion, that the intense nonlinear inverse cascade will effectively propagate the effects of the grid-scale dissipation of enstrophy to the large-scale dynamics. Conservation properties of the shallow water models, which we have considered in the context of an earlier test, are significantly better, but, pertaining to quantities defined in a different way, are not directly comparable to their nondivergent barotropic analogues.

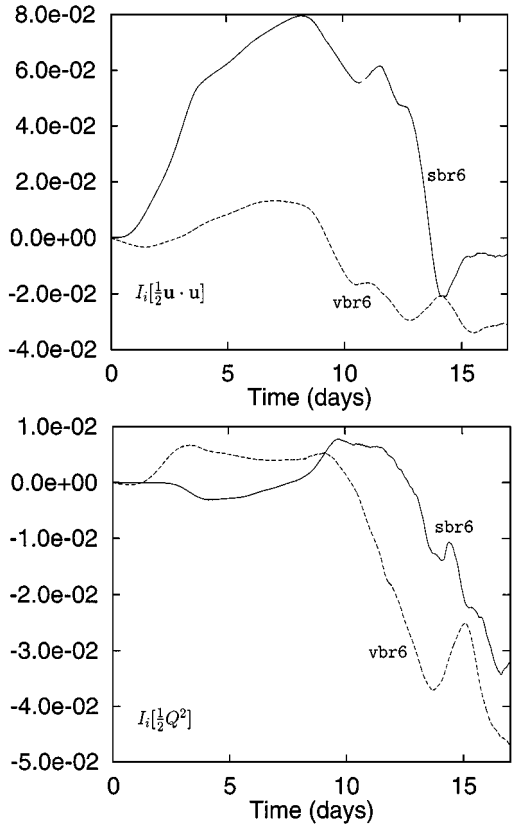

FIG. 10. Kinetic energy and potential enstrophy conservation results for `vbr6` and `sbr6` vortex erosion simulation.

6. CONCLUSIONS

The basic body of numerical methodology first employed in the Q-advecting nondivergent barotropic model of Stuhne and Peltier [1] has been successfully applied to the discretizations of scalar and vector formulations of more general one-layer fluid dynamic systems on the sphere (i.e., to shallow-water dynamics, as well as nondivergent barotropic dynamics). All of the resulting models, which we have denoted by the names `vbr`l, `sbr`l, `vsw`l, and `ssw`l, have been shown to be capable of resolving the complex dynamics involved in the process of polar stratospheric vortex erosion (see Juckes and McIntyre [4]). Such flows, being strongly nonlinear and involving the intense cascade of enstrophy to small scales, are very challenging computationally, and our results therefore suggest that the methodology under consideration is, in general, well-suited to the analysis of the full gamut of near-inviscid fluid dynamic phenomena. With the shallow water models `vsw`l and `ssw`l, we have also successfully simulated the simpler, but still important, physical configurations invoked in the standard test set of Williamson *et al.* [11]. Given these results and the fact that our basic methodology is very versatile in its applicability to different models and its extendibility to discretizations of arbitrary spatial dimension, we can conclude that it is likely to be well-suited to the general problem of simulating three-dimensional hydrodynamic flows in spherical shell geometry. This is clearly the goal towards which we are working.

Being based upon the same numerical components as those described in Stuhne and Peltier [1], all of the models we have discussed herein maintain the $\mathcal{O}(n)$ complexity in operation count per time step which we demonstrated in this previous paper. We have as yet expended very little effort to optimize the individual model codes employed, and so we will not discuss the absolute performance of these models in great detail but merely reiterate the result of Stuhne and Peltier [1] that an `sbr6` vortex erosion simulation runs at approximately 2.5 CPU seconds per time step on one processor of an SGI Challenge L server with a 150-MHz clock. Of greater interest is the relative performance of the various models and configurations considered. In this regard, the `vbr6` barotropic model has been found to be much less efficient, taking about 3.5 times as many CPU seconds per time step. This much poorer performance may be ascribed to the additional number of degrees of freedom which must be advanced in time and to the fact that the divergence correction term, ρ_i^{*l}, in the RHS of the elliptic height equation changes abruptly at leapfrog restart intervals (every tenth step), thus requiring more solver iterations. In contrast, the scalar shallow-water model, `ssw6`, takes only about 1.7 times the CPU time per step as `vbr6`. As expected, the vector version of the shallow water model, `vsw6`, is cheaper still, taking about 1.6 times the CPU time of the original model described in Stuhne and Peltier [1]. The fact that these last two figures are comparable, however, suggests that the requirement for iterative elliptic inversions at each step does not, in and of itself, necessarily result in a model which is *dramatically* less efficient. Performance would, of course, degrade further if more accuracy (and hence a greater number of iterations) were required, but usually only a few iterations (or even one) per time step are sufficient. This result that `ssw`*l* models need not be much less efficient than their `vsw`*l* counterparts implies, from our earlier discussion, that it may be of benefit to consider the implementation of semi-implicit time stepping in either model if it were to be employed as the basis of an actual production code.

We have found, on the basis of the shallow water test set results, that the accuracy of our `vsw5` model and the spatial distribution of its manifested numerical errors are both comparable to those of the `twig10242` model of Heikes and Randall [14, 15]. One or the other produces modestly better results depending upon the particular details of the case being analyzed. In comparing our two shallow water formulations, we have found that numerical predictions made with `ssw`*l* models tend to manifest similar quantitative error measures as those made with `vsw`*l* models, except in integrations of Charney balanced steady-state flows (where the latter models fare significantly better). The results from Test Case 1 and the spatial flow structures exhibited in Test Case 5 and in the simulations of polar vortex erosion all suggest that discretizations of the two different mathematical forms of the shallow-water equations exhibit slightly different "slow manifolds" in the sense of Leith [34]. There is no reason to prefer one or the other on this basis since there is no known physical rationale for a particular balance criterion to be imposed. However, for any given discretization, it will, of course, be of benefit to develop a specifically tailored balancing algorithm which will enable simulations to be initialized in computational steady states. The straightforward inversion of the Poisson problem in Eq. (17) which we employed all cases (except Test Case 7) has clearly proven to be better in this regard in its application to vector models. A suitable alternative for the scalar models would require additional effort in development.

In terms of other comparisons, the scalar `ssw`*l* models have shown modestly better enstrophy conservation properties, properties which could, no doubt, be further improved under time-stepping schemes which exploited the conservation equations of flux form governing

h^* and Q. Stuhne and Peltier [1] have already implemented a simple version of such a scheme for the nondivergent barotropic model, and substantially more sophisticated schemes may also be developed. Vector models are, in contrast, potentially extensible to simulate a wider class of nonhydrostatic 3D flows and can, if semi-implicit time-stepping is not used, avoid the need to solve elliptic problems at each time step. It would likely benefit applications of our methodology which do require the solution of the Poisson problem to refine this aspect of the numerical structure so as to achieve improved accuracy. The multigrid algorithm and smoother we have employed are by no means optimal for the 2-sphere, and better results might, no doubt, be obtained with some more sophisticated scheme. From the perspective of the application of this methodology to three-dimensional problems, however, it is sensible to focus the effort on a solver which is already known to have a direct 3D analogue. Beyond the elliptic inversion procedure, there are also further improvements which can be made in the other components of our numerical framework. One might, for instance, refine the numerical differentiation procedure to better take into account the slight local curvature of the sphere between adjacent grid points. As already discussed in Section 3.4, one might also experiment with alternative means of implementing spatial and temporal filters which eliminated some of the deficiencies of our present scheme. We are actively considering these and other refinements as possible means of improving the methodology. Even as it stands, however, this methodology has been shown to produce competitive results (as compared, specifically, with the model of Heikes and Randall [14, 15]).

REFERENCES

1. G. R. Stuhne and W. R. Peltier, Vortex erosion and amalgamation in a new model of large scale flow on the sphere, *J. Comput. Phys.* **128**, 58 (1996).
2. W. Hackbusch, *Multi-Grid Methods and Applications, Springer Series in Computational Mathematics*, Vol. 4 (Springer-Verlag, Berlin, 1985).
3. J. Pedlosky, *Geophysical Fluid Dynamics*, 2nd ed. (Springer-Verlag, New York, 1987).
4. M. N. Juckes and M. E. McIntyre, A. high resolution one-layer model of breaking planetary waves in the stratosphere, *Nature* **328**, 13 (1987).
5. S. A. Orszag, Fourier series on spheres, *Mon. Weather Rev.* **102**, 56 (1974).
6. J. R. Driscoll and D. M. Healy, Computing Fourier-transforms and convolutions on the 2-sphere, *Adv. Appl. Math.* **15**, 202 (1994).
7. M. Hortal and A. J. Simmons, Use of reduced Gaussian grids in spectral models, *Mon. Weather Rev.* **119**, 1057 (1991).
8. D. Williamson, Integration of the barotropic vorticity equation on a spherical geodesic grid, *Tellus* **20**, 642 (1968).
9. R. Sadourny, A. Arakawa, and Y. Mintz, Integration of the nondivergent barotropic vorticity equation with an icosahedral-hexagonal grid on the sphere, *Mon. Weather Rev.* **96**, 351 (1968).
10. J. R. Baumgardner and P. O. Frederickson, Icosahedral discretization of the two-sphere, *Siam J. Numer. Anal.* **22**, 1107 (1985).
11. D. L. Williamson, J. B. Drake, J. J. Hack, R. Jakob, and P. N. Swarztrauber, A standard test set for numerical approximations to the shallow water equations in spherical geometry, *J. Comput. Phys.* **102**, 211 (1992).
12. M. J. P. Cullen, Integrations of the primitive equations on a sphere using the finite element method, *Quart. J. R. Met. Soc.* **100**, 555 (1974).
13. Y. Masuda and H. Ohnishi, An integration scheme of the primitive equation model with an icosahedral-hexagonal grid system and its application to the shallow water equations, in *Short- and Medium-Range Numerical Weather Prediction: Collection of Papers Presented at the WMO/IUGG NWP Symposium, Tokyo, August 4–8, 1986* (Japan Meteorological Society, Tokyo, 1986), p. 317.

14. R. Heikes and D. A. Randall, Numerical integration of the shallow water equations on a twisted icosahedral grid. Part I. Basic design and results of rates, *Mon. Weather Rev.* **123**, 1862 (1995).
15. R. Heikes and D. A. Randall, Numerical integration of the shallow water equations on a twisted icosahedral grid. Part II. A detailed description of the grid and an analysis of numerical accuracy, *Mon. Weather Rev.* **123**, 1881 (1995).
16. J. M. Augenbaum and C. S. Peskin, On the construction of the Voronoi mesh on a sphere, *J. Comput. Phys.* **14**, 177 (1985).
17. P. N. Swarztrauber, D. L. Williamson, and J. B. Drake, The Cartesian method for solving partial differential equations in spherical geometry, *Dyn. Atmos. Oceans* **27**, 679 (1997).
18. W. Bourke, A multi-level spectral model. I. Formulation and hemispheric integrations, *Mon. Weather Rev.* **102**, 687 (1974).
19. B. J. Hoskins and A. J. Simmons, A multi-layer spectral model and the semi-implicit method, *Quart. J. R. Met. Soc.* **101**, 637 (1975).
20. A. C. DeVerdière and R. Schopp, Flows in a rotating spherical shell: the equatorial case, *J. Fluid Mech.* **276**, 233 (1994).
21. J. Côté, A Lagrange multiplier approach for the metric terms of semi-Lagrangian models on the sphere, *Quart. J. R. Met. Soc.* **114**, 1347 (1988).
22. R. Ford, Gravity wave radiation from vortex trains in rotating shallow water, *J. Fluid Mech.* **281**, 81 (1994).
23. M. J. Lighthill, On sound generated aeordynamically, I. General Theory, *Proc. R. Soc. London A* **211**, 564 (1952).
24. M. Kwizak and A. J. Robert, A semi-implicit scheme for grid point atmospheric models of the primitive equations, *Mon. Weather Rev.* **99**, 32 (1971).
25. A. J. Robert, J. Henderson, and C. Turnbull, An implicit time integration scheme for baroclinic models of the atmosphere, *Mon. Weather Rev.* **100**, 329 (1972).
26. J. G. Charney, The use of the primitive equations in numerical prediction, *Tellus* **7**, 22 (1955).
27. E. B. Becker, G. F. Carey, and J. T. Oden, *Finite Elements: An Introduction* (Prentice–Hall, Englewood Cliffs, NJ, 1981), Vol. 1.
28. S. R. Karpik and W. R. Peltier, Multigrid methods for the solution of Poisson's equation in a thick spherical shell, *SIAM J. Sci. Stat. Comput.* **12**, 681 (1991).
29. P. D. Lax and B. Wendroff, Systems of conservation laws, *Comm. Pure and Appl. Math.* **13**, 217 (1960).
30. G. J. Haltiner, *Numerical Weather Prediction* (Wiley, New York, 1971).
31. G. L. Browning, J. J. Hack, and P. N. Swarztrauber, A comparison of three numerical methods for solving differential equations on the sphere, *Mon. Weather Rev.* **117**, 1058 (1989).
32. R. Asselin, Frequency filter for time integrators, *Mon. Weather Rev.* **100**, 487 (1972).
33. R. Jakob-Chien, J. J. Hack, and D. L. Williamson, Spectral transform solutions to the shallow water test set, *J. Comput. Phys.* **119**, 164 (1995).
34. C. Leith, Nonlinear normal mode initialization and quasi-geostrophic theory, *J. Atmos. Sci.* **37**, 958 (1980).
35. M. E. McIntyre and W. A. Norton, Potential vorticity inversion on a hemisphere, preprint.
36. M. N. Juckes, A shallow water model of the winter stratosphere, *J. Atmos. Sci.* **46**, 2934 (1989).